ARTICLE

Light-sensitive phosphorylation regulates retinal IMPDH1 activity and filament assembly

S. John Calise[1], Audrey G. O'Neill[1], Anika L. Burrell[1], Miles S. Dickinson[1], Josephine Molfino[1], Charlie Clarke[1], Joel Quispe[1], David Sokolov[1], Rubén M. Buey[2], and Justin M. Kollman[1]

Inosine monophosphate dehydrogenase (IMPDH) is the rate-limiting enzyme in guanosine triphosphate (GTP) synthesis and assembles into filaments in cells, which desensitizes the enzyme to feedback inhibition and boosts nucleotide production. The vertebrate retina expresses two splice variants IMPDH1(546) and IMPDH1(595). In bovine retinas, residue S477 is preferentially phosphorylated in the dark, but the effects on IMPDH1 activity and regulation are unclear. Here, we generated phosphomimetic mutants to investigate structural and functional consequences of S477 phosphorylation. The S477D mutation resensitized both variants to GTP inhibition but only blocked assembly of IMPDH1(595) filaments. Cryo-EM structures of both variants showed that S477D specifically blocks assembly of a high-activity assembly interface, still allowing assembly of low-activity IMPDH1(546) filaments. Finally, we discovered that S477D exerts a dominant-negative effect in cells, preventing endogenous IMPDH filament assembly. By modulating the structure and higher-order assembly of IMPDH, S477 phosphorylation acts as a mechanism for downregulating retinal GTP synthesis in the dark when nucleotide turnover is decreased.

Introduction

Photoreceptor cells in the retina require high levels of guanine nucleotides to meet the metabolic demands of cyclic guanosine monophosphate (cGMP) signaling. To maintain nucleotide levels, they activate the de novo purine synthesis pathway to supplement nucleotides supplied by salvage pathways. Purine synthesis is a critical metabolic hub, and enzymes in the pathway are under tight control by various modes of regulation, including feedback inhibition, allostery (Buey et al., 2015), biomolecular condensation (Pedley et al., 2022a), posttranslational modification (Liu et al., 2019), oligomerization and polymerization, and assembly of polymers into micron-scale subcellular structures known as metabolic filaments (Hvorecny and Kollman, 2023; Lynch et al., 2020; Park and Horton, 2019; Simonet et al., 2020).

The de novo purine synthesis pathway yields inosine monophosphate (IMP), the precursor for adenine and guanine nucleotides. IMP dehydrogenase (IMPDH) is the rate-limiting enzyme in guanosine triphosphate (GTP) synthesis (Fig. 1 A). In humans, IMPDH has two canonical 514-residue isoforms with 84% sequence identity and similar kinetics (Carr et al., 1993). IMPDH1 is expressed at low levels in most tissues, while IMPDH2 is upregulated in proliferating and transformed cells

(Collart et al., 1992; Jackson et al., 1975; Nagai et al., 1992; Senda and Natsumeda, 1994). IMPDH is regulated by GTP and ATP, which compete for three nucleotide binding sites in the regulatory Bateman domain to inhibit or activate the enzyme, respectively (Buey et al., 2022). In solution, IMPDH forms a catalytic tetramer that reversibly dimerizes upon nucleotide binding to form a functional octamer, which can assemble endon-end to form polymers (referred to as "filaments" here). GTP binds nucleotide binding sites 2 and 3, while ATP binds site 1 and competes with GTP for site 2 (Fig. 1 B) (Buey et al., 2015, 2017; Johnson and Kollman, 2020).

Binding of GTP and ATP controls the polymerization of IMPDH in vitro. The presence of ATP in sites 1 and 2 promotes filaments composed of octamers in an extended, high-activity state, while GTP in sites 2 and 3 leads to filaments containing compressed, less active octamers (Fig. 1, C and D) (Anthony et al., 2017; Burrell et al., 2022; Johnson and Kollman, 2020). For IMPDH2, filament assembly maintains a "flat" conformation of the catalytic tetramer that prevents full inhibition of the enzyme within the filament, allowing the enzyme to remain partially active in vitro (Fernández-Justel et al., 2019; Johnson and Kollman, 2020). In cells, single IMPDH filaments bundle

[1]Department of Biochemistry, University of Washington, Seattle, WA, USA; [2]Metabolic Engineering Group, Departamento de Microbiología y Genética, Universidad de Salamanca, Campus Miguel de Unamuno, Salamanca, Spain.

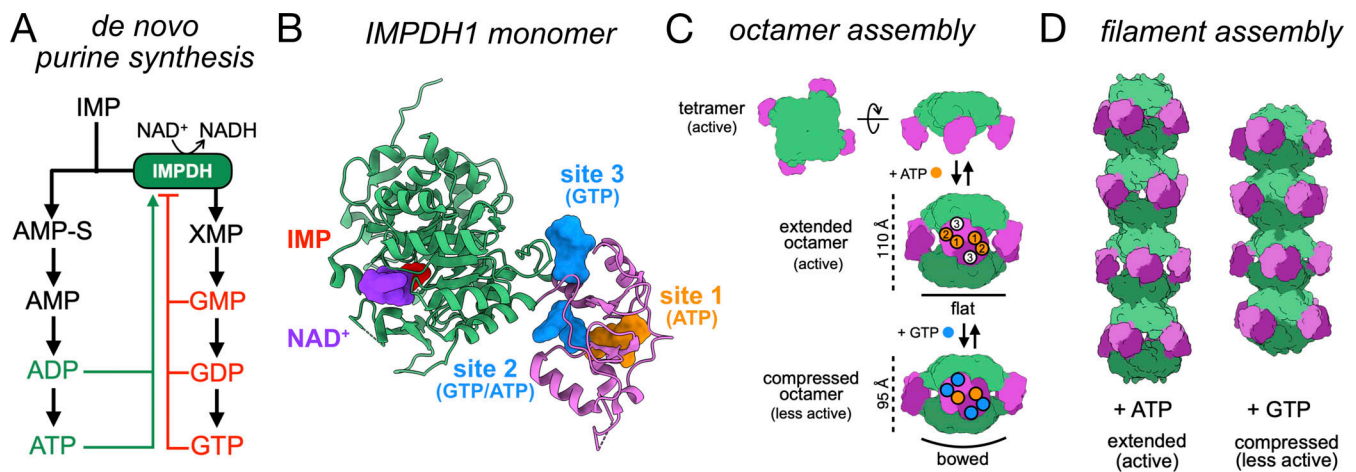Correspondence to Justin M. Kollman: jkoll@uw.edu.

Figure 1. **IMPDH function, structure, and regulation. (A)** In the de novo purine synthesis pathway, IMP is converted to adenine or guanine nucleotides. IMPDH converts IMP to xanthosine monophosphate (XMP) in the rate-limiting step of GMP synthesis. Adenine and guanine nucleotides activate or inhibit IMPDH, respectively. **(B)** The IMPDH monomer (PDB: 7RGD) binds IMP (red) and NAD+ (purple) in the active site of the catalytic domain (green). ATP (orange) and GTP (blue) can bind in allosteric nucleotide binding sites in the Bateman domain (pink). **(C)** IMPDH is in equilibrium between tetramer and octamer in solution. Octamers form through interactions of the Bateman domains from opposing tetramers. The catalytic tetramer can adopt a flat or bowed conformation. Binding of nucleotides to the Bateman domain promotes either an extended, active or compressed, less active octamer conformation. **(D)** Octamers assemble end-on-end to form filaments that can accommodate both extended and compressed conformations.

together to form micron-scale ultrastructures (Juda et al., 2014; Schiavon et al., 2018; Thomas et al., 2012). IMPDH filament assembly in vivo correlates with metabolic conditions that require high GTP levels, like T cell activation and the rapid proliferation of stem cells (Calise and Chan, 2020; Calise et al., 2018; Carcamo et al., 2011; Duong-Ly et al., 2018; Keppeke et al., 2018).

IMPDH1 is the dominant isoform in the vertebrate retina and is expressed as two tissue-specific splice variants (Bowne et al., 2006a; Hedstrom, 2009). IMPDH1(546) has a disordered extension of 37 residues that replace the five canonical residues at the C-terminus. IMPDH1(595) contains the same C-terminal extension plus 49 residues at the N-terminus (Fig. 2 A) (Burrell and Kollman, 2022; Spellicy et al., 2007). IMPDH1(546) and IMPDH1(595) are less sensitive to GTP inhibition compared with the canonical enzyme IMPDH1(514), enabling increased GTP production to meet the significant demands of cGMP signaling in photoreceptor cells (Fig. 2 B) (Andashti et al., 2020, 2021; Burrell et al., 2022; Plana-Bonamaisó et al., 2020). Within IMPDH1(514) and IMPDH1(546) filaments, the assembly interface between two octamers can adopt two conformations referred to as the large and small interfaces, which correlate with high and low enzymatic activity, respectively (Burrell et al., 2022). For IMPDH1(595), the N-terminal extension locks it in the large interface, which stabilizes a more active conformation of the enzyme and contributes to increased resistance to GTP inhibition compared with the canonical enzyme (Fig. 2 C) (Burrell et al., 2022).

The importance of IMPDH1 in retinal function is reflected in the multiple missense mutations that have been linked to gradual vision loss caused by autosomal dominant retinitis pigmentosa (Bowne et al., 2002, 2006b; Grover et al., 2004; Kennan et al., 2002; Wada et al., 2005) and Leber congenital amaurosis (Bowne et al., 2006b). None of the mutations alter

canonical IMPDH1 catalytic activity in vitro (Aherne et al., 2004; Mortimer and Hedstrom, 2005; Xu et al., 2008), but we recently showed that some mutations alter the architecture of IMPDH retinal variant filaments, disrupting regulation by GTP and providing clues as to why clinical manifestations are limited to the retina (Burrell et al., 2022).

Recent phosphoproteomic analyses of bovine retinas identified three phosphorylation sites in IMPDH1 associated with light and dark states (Plana-Bonamaisó et al., 2020). Phosphorylation occurs at T159/S160, residues directly involved with allosteric nucleotide binding site 1, in response to light. This desensitizes the enzyme to GTP regulation, allowing elevated GTP pools for phototransduction. Phosphorylation at S416, a residue on a mobile flap in the catalytic domain required for catalysis, was observed in both light and dark states. The third site S477 is preferentially phosphorylated in the dark, but its effects on reaction kinetics and GTP regulation are unclear. An S477D phosphomimetic mutant of IMPDH1(546) had similar reaction kinetics to wildtype (WT) in the absence of nucleotides, and GTP regulation of IMPDH1(514)-S477D appeared similar to WT canonical enzyme, although no data on the GTP inhibition of S477D mutant retinal variants were shown (Plana-Bonamaisó et al., 2020). Phosphorylation at S477 was speculated to disrupt filament formation (Plana-Bonamaisó et al., 2020).

Here, we show that S477D disrupts assembly of the large, high-activity filament interface, completely preventing IMPDH1(595) filament assembly and forcing IMPDH1(546) filaments into the small, lower-activity interface. These changes in higher-order structure correspond to increased sensitivity to GTP inhibition and lower reaction velocity in enzyme assays. This suggests that phosphorylation directly affects flux through IMPDH1 by preventing its ability to form high-activity filaments, introducing an additional mechanism for controlling enzyme filament formation to tune metabolic activity.
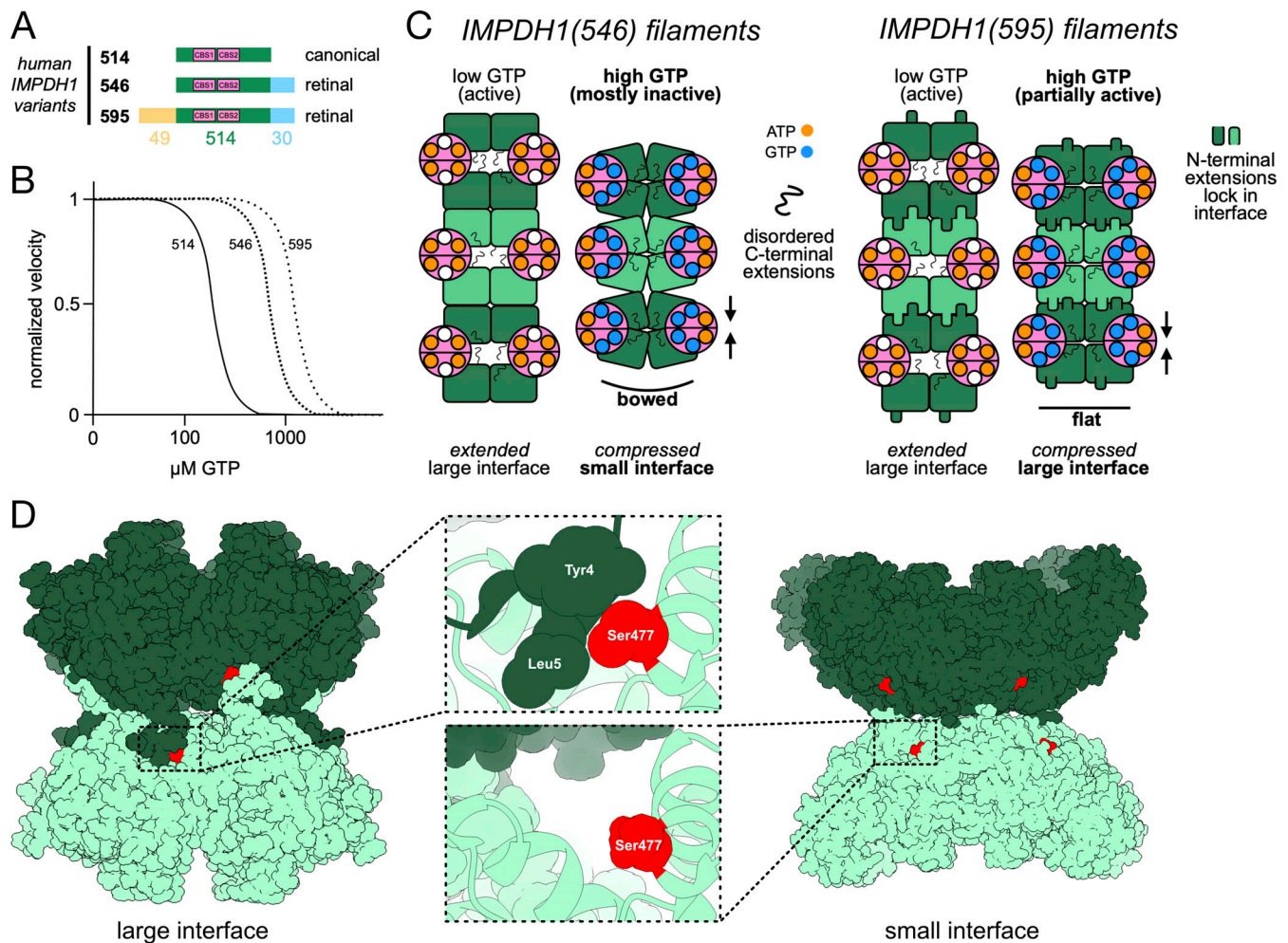
Figure 2. **Human IMPDH1 retinal variants. (A)** Schematic of human IMPDH1 variant structures. Pink: tandem cystathionine-β-synthase (CBS) domains (Bateman domain). Blue: C-terminal extension. Gold: N-terminal extension. **(B)** Schematic (for illustrative purposes only) of the relationship between the half-maximal inhibitory concentration (IC$_{50}$) for GTP for the IMPDH1 variants based on published data (Burrell et al., 2022). Data were previously generated under the same assay conditions as the current study (see Materials and methods). **(C)** Binding of ATP (orange) to IMPDH1(546) drives assembly of filaments containing extended octamers that are mostly active and connected with the large interface. GTP (blue) binding promotes a filament of less active, compressed octamers in a bowed conformation with the small interface. ATP also drives filament assembly of active, extended IMPDH1(595) octamers with the large interface. However, when GTP is present, the N-terminal extensions on the IMPDH1(595) filament maintain the flat conformation and large interface, resisting inhibition and remaining more active than IMPDH1(546). **(D)** Location of Ser477 (red) in both the large (PDB: 7RER) and small interfaces (PDB: 7RFE).

Results

S477D disrupts IMPDH1(595) filament assembly in vitro

We examined purified S477D variants IMPDH1(595)-S477D and IMPDH1(546)-S477D by negative stain electron microscopy (EM) in the presence of no ligand (Apo) or either 1 mM ATP or 1 mM GTP, which promote polymerization of the WT enzyme (Burrell et al., 2022; Johnson and Kollman, 2020). S477D completely prevented assembly of IMPDH1(595) filaments, allowing only free octamer formation in the presence of ATP or GTP (Fig. 3 A). At this resolution, higher-order assembly of IMPDH1(546)-S477D appeared unaffected, assembling octamers and polymers similar to WT enzyme (Fig. 3 B). S477D also partially prevented polymerization of the canonical IMPDH1(514), although the effects were not as clear as in the retinal variants (Fig. S1). Previous structures of IMPDH1 filaments showed that S477 contacts the N-terminus of the opposing monomer in the large interface, but

makes no contacts in the small interface, suggesting phosphorylation at S477 is likely to specifically break the large interface (Fig. 2 D). Thus, we suspected that the IMPDH1(546)-S477D filaments we observed by negative stain were in the small interface. Complete disassembly of IMPDH1(595) filaments supports our previous structural data showing that IMPDH1(595) filament assembly is restricted to the large interface (Burrell et al., 2022).

S477D resensitizes both retinal variants to GTP inhibition

WT retinal variants IMPDH1(546)-WT and IMPDH1(595)-WT are significantly less sensitive to GTP inhibition compared with the canonical IMPDH1(514) (Burrell et al., 2022). Here, we wanted to test the S477D mutants for any effects on GTP regulation of activity. In both retinal variants, S477D resensitized the enzyme to GTP inhibition. S477D decreases the half-maximal
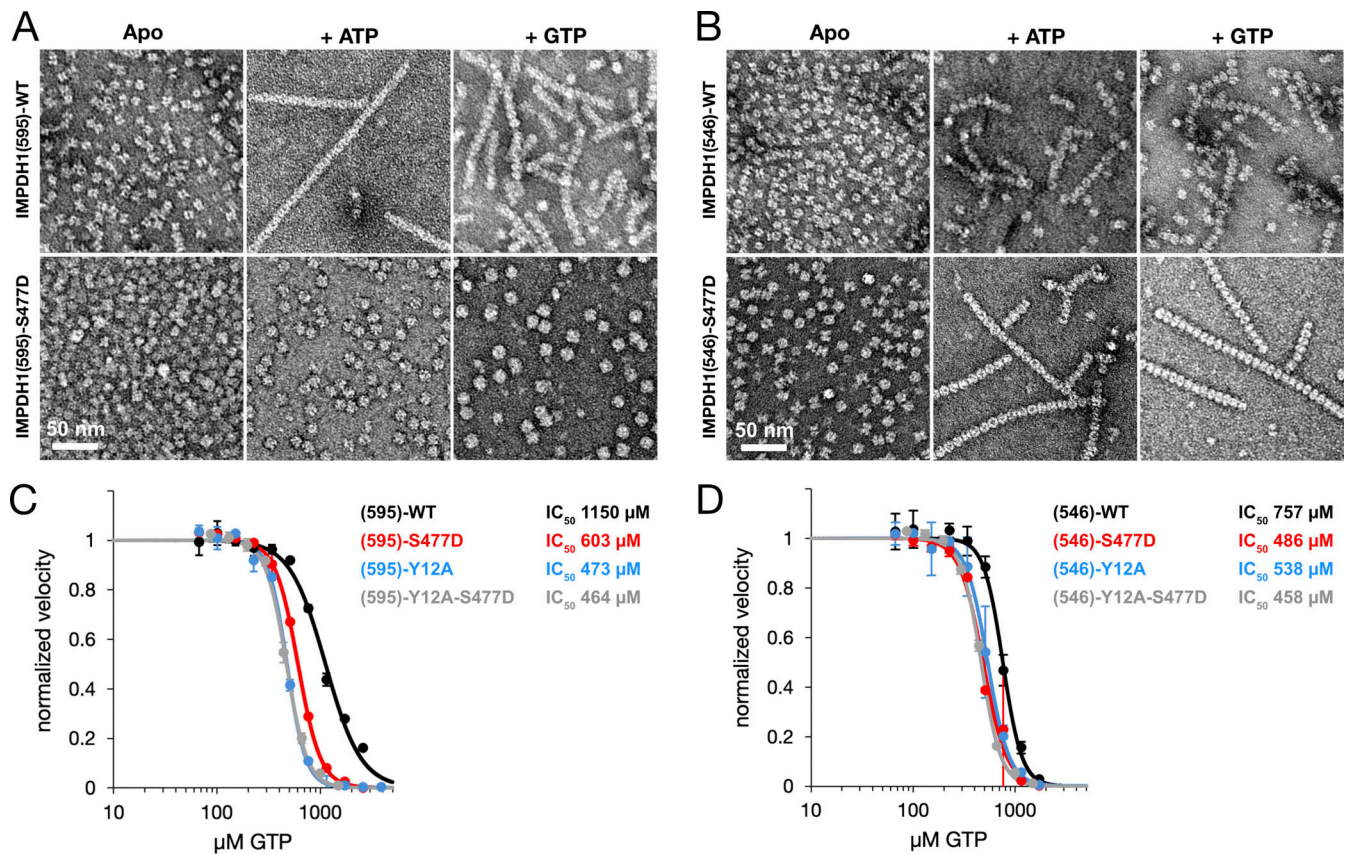
Figure 3. **S477D disrupts IMPDH1(595) filament assembly and resensitizes both variants to GTP inhibition. (A)** Negative stain EM of 1 µM IMPDH1(595)-WT and 1 µM IMPDH1(595)-S477D under Apo, +1 mM ATP, or +1 mM GTP conditions. **(B)** Negative stain EM of 1 µM IMPDH1(546)-WT and 1 µM IMPDH1(546)-S477D under the same conditions. **(C)** GTP inhibition curve of IMPDH1(595)-S477D (red) compared to WT (black), Y12A (blue), and Y12A-S477D (gray). **(D)** GTP inhibition curve of IMPDH1(546)-S477D (red) compared to WT (black), Y12A (blue), and Y12A-S477D (gray). For GTP inhibition assays, reactions were performed in triplicate ($n = 3$) and each data point represents a mean value with error bars depicting SD. Reactions included 1 µM enzyme, 1 mM ATP, 1 mM IMP, 300 µM NAD$^+$, and varying concentrations of GTP.

inhibitory concentration (IC$_{50}$) for GTP in IMPDH1(595) and IMPDH1(546) to the same extent as the engineered mutation Y12A, which also disrupts filament assembly (Fig. 3, C and D) (Anthony et al., 2017; Burrell et al., 2022; Fernández-Justel et al., 2019; Johnson and Kollman, 2020). Enzyme assays are summarized in Table 1.

Inhibition of IMPDH1 involves two conformational changes: interdomain movements that switch from an extended to compressed octamer and transition of the catalytic tetramer from a flat conformation to a bowed conformation at the filament assembly interface (Burrell et al., 2022; Johnson and Kollman, 2020). The large interface is associated with stabilizing the flat conformation, leading to higher catalytic activity, while the small interface is associated with the bowed conformation and lower activity. In completely breaking IMPDH1(595) filament assembly, S477D removes the enzyme's ability to engage the large interface and stabilize the flat conformation. Free IMPDH octamers adopt the compressed and bowed conformation upon GTP binding, leading to lower activity (Burrell et al., 2022; Johnson and Kollman, 2020), explaining the increased sensitivity to GTP inhibition of IMPDH1(595)-S477D in our assays. However, why IMPDH1(546)-S477D was resensitized to the levels of the engineered filament-disrupting mutation Y12A was

not clear. To gain further insights into structural details, we turned to cryogenic EM (cryo-EM).

IMPDH1(595)-S477D free octamer adopts a bowed conformation

First, we solved a 3.1 Å cryo-EM structure of the IMPDH1(595)-S477D free octamer in the presence of GTP, ATP, IMP, and NAD$^+$ (Fig. 4 A and Fig. S2). We built an atomic model and aligned it with a previous model (Protein Data Bank [PDB]: 7RGD) of IMPDH1(595)-WT under the same ligand conditions in a compressed state within a filament. We observed no significant changes in the conformation of the backbone, with a calculated root-mean-square deviation (RMSD) of alpha carbons when aligned on chain A of both structures of 0.6 Å. We then took a closer look at the catalytic tetramer of each model to determine if IMPDH1(595)-S477D was in the flat or bowed conformation (Fig. 4 B). We aligned S477D and WT tetramers on chain A and observed a 3° shift in chain C (the monomer positioned diagonally across the tetramer) of S477D relative to WT, showing that IMPDH1(595)-S477D free octamer adopts a bowed conformation similar to the inhibited canonical IMPDH1(514)-WT within a filament (RMSD of alpha carbons when aligned on chain A of IMPDH1(595)-S477D versus inhibited IMPDH1(514)-WT = 0.7 Å).

Table 1. Summary of enzyme inhibition assays from Fig. 1

Enzyme	IC_{50} GTP (µM) best-fit	IC_{50} GTP (µM) 90% confidence interval	Hill best-fit	Hill 90% confidence interval
IMPDH1(595)-WT	1,150	1,040–1,230	2.3	2.2–3.0
IMPDH1(595)-S477D	603	590–631	3.7	3.5–4.5
IMPDH1(595)-Y12A	473	462–492	4.5	4.2–5.5
IMPDH1(595)-Y12A-S477D	464	458–486	4.1	3.9–5.0
IMPDH1(546)-WT	757	725–792	4.6	3.9–5.7
IMPDH1(546)-S477D	486	452–524	3.7	3.0–4.9
IMPDH1(546)-Y12A	538	505–575	4.0	3.3–5.3
IMPDH1(546)-Y12A-S477D	458	450–480	4.2	4.0–5.1

IMPDH1(595)-WT is stabilized in the large interface and flat conformation in the filament by its extended N-terminus (Burrell et al., 2022). The extended N-terminus was unresolved in our map of the free octamer, suggesting it only becomes ordered upon interaction with a binding partner.

Both inhibited and active IMPDH1(546)-S477D filaments assemble with the small interface

Next, we solved a 3.3 Å cryo-EM structure of the IMPDH1(546)-S477D compressed octamer within a filament in the presence of GTP, ATP, IMP, and NAD⁺ (Fig. 5 A and Fig. S3). We built an atomic model of the compressed octamer and compared it with a previous model (PDB: 7RGQ) of IMPDH1(546)-WT in a

compressed state within a filament, which adopts the small interface (Burrell et al., 2022). Aligning these two models showed no significant differences between single protomers or octamers (RMSD of alpha carbons when aligned on chain A of both structures = 0.5 Å). From the same dataset, we separately determined a structure of the filament assembly interface by centering the reconstruction on the D4 symmetry center between octamers in the filament, an approach we have used in the past to yield the highest resolution reconstructions of the interface (Burrell et al., 2022; Johnson and Kollman, 2020). This approach yielded a 3.3 Å structure of the assembly contacts, which is essentially identical to the IMPDH1(546)-WT assembly interface (RMSD of alpha carbons when aligned on chain A of both structures = 0.6 Å) (Fig. 5 C; and Fig. 6, A and B). Thus, at the level of protomer, octamer, and filament, the S477D mutation does not affect the structure of fully inhibited IMDPH1(546).

In the active state in the presence of ATP, IMP, and NAD⁺, IMPDH1(546)-WT assembles a filament with a large interface (Burrell et al., 2022). We solved a 2.4 Å cryo-EM structure of IMPDH1(546)-S477D under the same conditions (Fig. 5 B and Fig. S4) and aligned the model to IMPDH1(546)-WT in an extended state within a filament (PDB: 7RGM). Individual protomers appeared highly similar (RMSD of alpha carbons when aligned on chain A of both structures = 0.6 Å), but when we aligned octamers on chain A, we detected a 3° shift in the protomer on the opposite side of the octamer. We solved a 2.1 Å interface-centered structure of IMPDH1(546)-S477D and compared the filament assembly interface with IMPDH1(546)-WT (Fig. 6, C and D). The IMPDH1(546)-S477D extended, active filament adopts the small interface driven by contacts between Y12 and E487 (Fig. 5 D, top). This is significantly different from the IMPDH1(546)-WT large interface, which has a relative 41° rotation with R356 contacting Y12 (Fig. 5 D, bottom). We then aligned active IMPDH1(546)-WT, inhibited IMPDH1(546)-WT, and active IMPDH1(546)-S477D to compare their catalytic tetramer conformations. The catalytic tetramer of active

A IMPDH1(595)-S477D GTP + ATP

compressed

B inhibited IMPDH1(595)-S477D vs. inhibited IMPDH1(595)-WT

3°

chain A   chain C
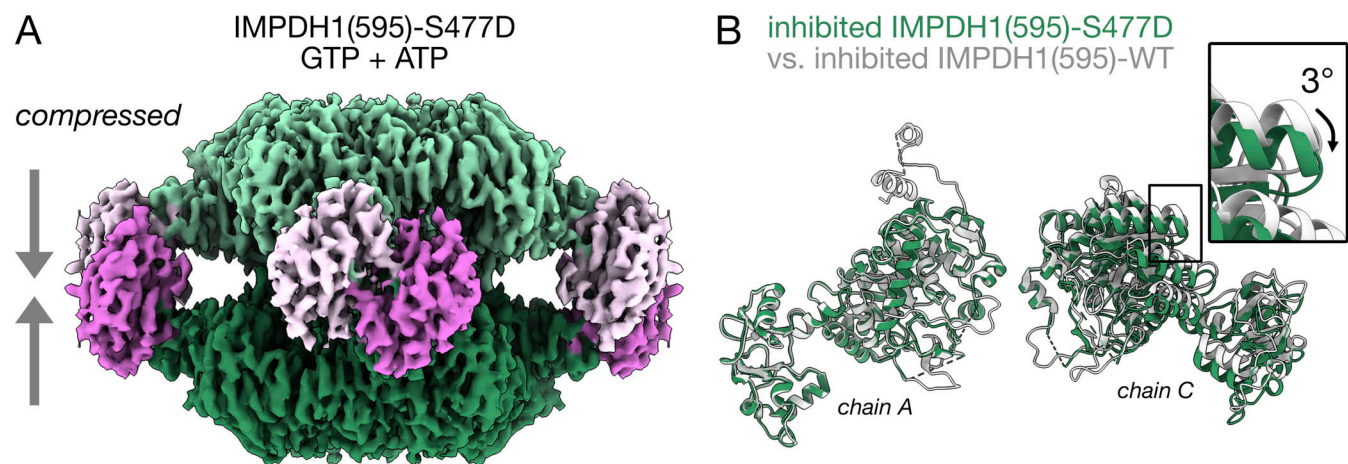
Figure 4. **Cryo-EM structure of the IMPDH1(595)-S477D free octamer. (A)** Cryo-EM map (3.1 Å) of the compressed IMPDH1(595)-S477D free octamer under inhibitory conditions, in the presence of GTP, ATP, IMP, and NAD⁺. **(B)** Alignment of the atomic model built from the map in panel A (green) with the previously built model of IMPDH1(595)-WT (gray, PDB: 7RGD). Chains A and C are shown, which are positioned diagonally across from each other in the IMPDH1 catalytic tetramer. The S477D catalytic tetramer is in a bowed conformation, bent ∼3° relative to the flat conformation of the WT. RMSD of alpha carbons when aligned on chain A of both structures = 0.6 Å.
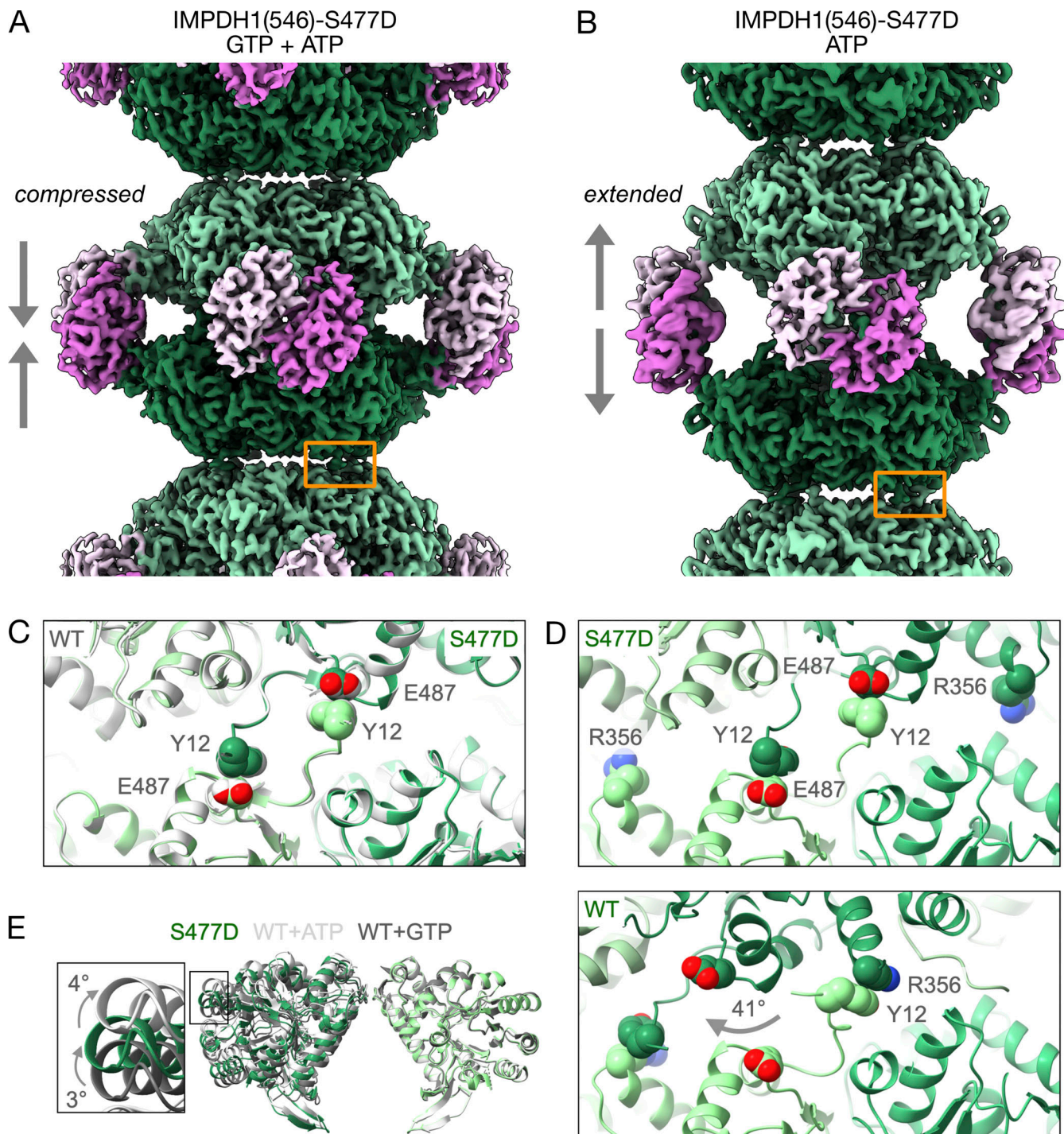
Figure 5. **Cryo-EM structures of IMPDH1(546)-S477D in inhibited and active states. (A)** Cryo-EM map (3.3 Å) of a compressed IMPDH1(546)-S477D octamer within a filament, in the presence of GTP, ATP, IMP, and NAD⁺. Orange box: assembly interface shown in panel C. **(B)** Cryo-EM map (2.4 Å) of an extended IMPDH1(546)-S477D octamer within a filament, in the presence of ATP, IMP, and NAD⁺. Orange box: assembly interface shown in panel D. **(C)** Assembly interface of the compressed IMPDH1(546)-S477D filament (green) aligned to compressed IMPDH1(546)-WT (gray, PDB: 7RGI). In both S477D and WT, the interaction between Y12 and E487 drives filament assembly. **(D)** Extended IMPDH1(546)-S477D filament assembly interface (top) compared with the extended IMPDH1(546)-WT interface (bottom, PDB: 7RGL). Top: Like the compressed 546 filament, Y12 and E487 drive assembly of the extended 546 filaments. Bottom: In the extended 546-WT filament, Y12 and R356 interact to drive assembly. **(E)** Active IMPDH1(546)-WT (light gray), active IMPDH1(546)-S477D (green), and inactive IMPDH1(546)-WT (dark gray) aligned on the right monomer. S477D adopts an intermediate conformation between the fully bowed and flat conformations.

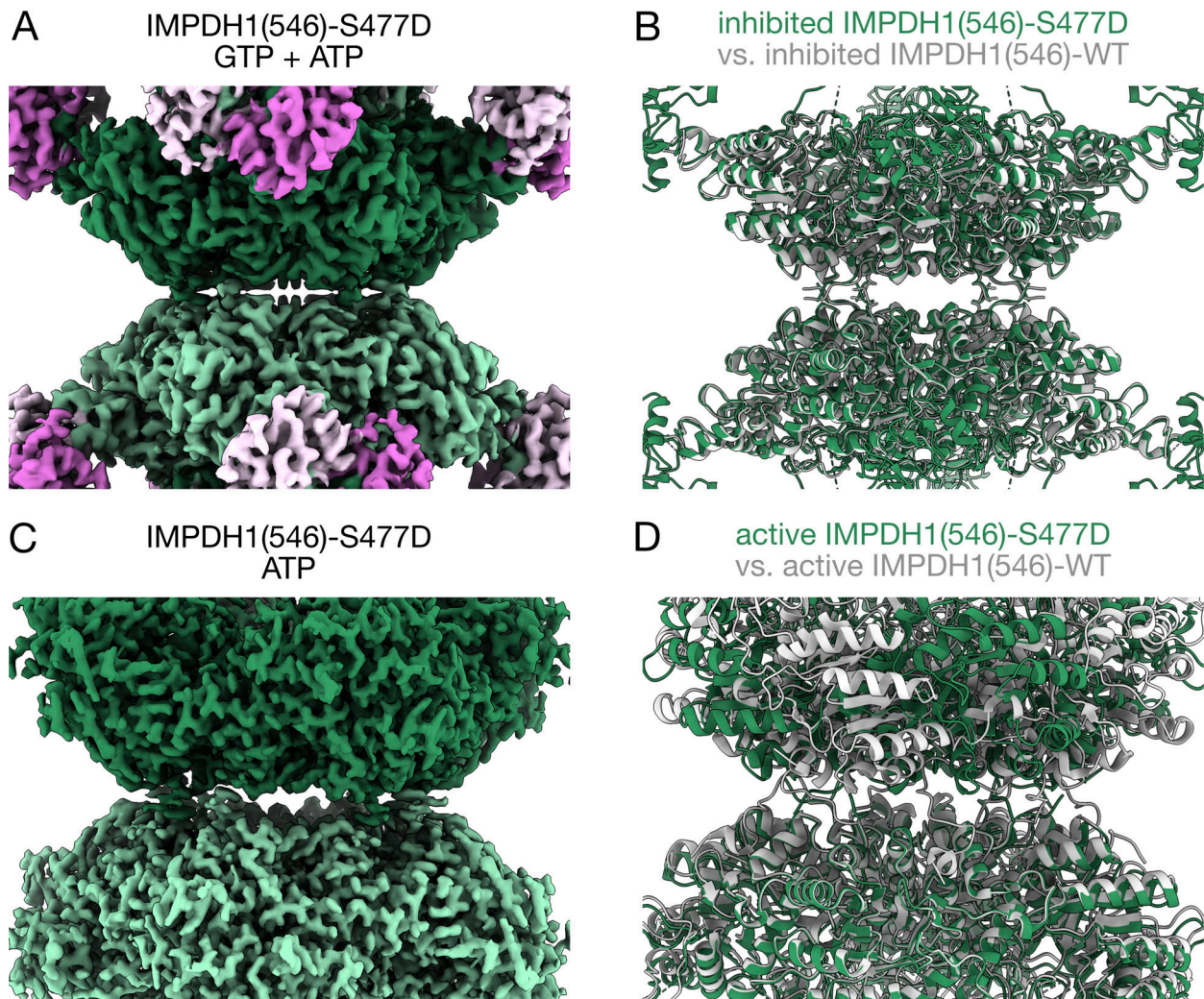Figure 6. **Interface-centered structures of inhibited and active IMPDH1(546)-S477D. (A)** Cryo-EM map (3.3 Å) of the filament assembly interface between two compressed IMPDH1(546)-S477D octamers, in the presence of GTP, ATP, IMP, and NAD⁺. **(B)** Model of inhibited IMPDH1(546)-S477D (green) aligned to inhibited IMPDH1(546)-WT (gray). RMSD of alpha carbons when aligned on chain A of both structures = 0.6 Å. **(C)** Cryo-EM map (2.1 Å) of the filament assembly interface between two extended IMPDH1(546)-S477D octamers, in the presence of ATP, IMP, and NAD⁺. **(D)** Model of active IMPDH1(546)-S477D (green) aligned to active IMPDH1(546)-WT (gray). Aligned on chain A of both structures.

IMPDH1(546)-S477D adopts a unique intermediate conformation between bowed and flat (Fig. 5 E, inset). Forming the small interface with an intermediate tetramer conformation suggests the enzyme may be primed to enter the compressed, bent state when GTP is present, lowering the transition barrier and effectively raising the affinity for GTP. In a kinetics assay, this would mean IMPDH1(546)-S477D is more sensitive to GTP inhibition, as we detected in Fig. 3 D.

S477D is a dominant-negative regulator of IMPDH filament assembly

Given the obvious disruption to higher-order assembly of IMPDH1(595)-S477D, we wanted to investigate the impact of the phosphomimetic on filament assembly in cells. We transfected HeLa cells with expression constructs encoding FLAG-tagged WT, S477D mutant, and S477A mutant retinal variants (Fig. 7). After 48 h, we treated cells with 1 mM ribavirin for 2 h, which led to robust IMPDH filament assembly in nearly 100% of cells

(Calise et al., 2016; Carcamo et al., 2011; Covini et al., 2012; Keppeke et al., 2015). We then fixed and stained cells with an anti-IMPDH2 antibody to label endogenous IMPDH and anti-FLAG antibody to label transfected protein.

Both WT and S477A variants assembled typical micron-scale filaments in a high percentage of transfected cells, as expected (595-WT: 98%, 595-S477A: 98%, 546-WT: 98%, 546-S477A: 100%). However, S477D exerted a dominant-negative effect, blocking essentially all filament assembly by endogenous IMPDH in transfected cells (595-S477D: 2%, 546-S477D: 2%). In cell populations transfected with S477D mutants, filaments can be observed in adjacent non-transfected cells as an internal control (white arrows, Fig. 7). Since overexpression alone also causes IMPDH1 filament assembly (Gunter et al., 2008; Keppeke et al., 2018, 2023), we performed the same experiment without ribavirin treatment and observed similar results (Fig. S5).

These data suggest an important point: IMPDH1(546)-S477D forms filaments in vitro but only with the small interface, so its
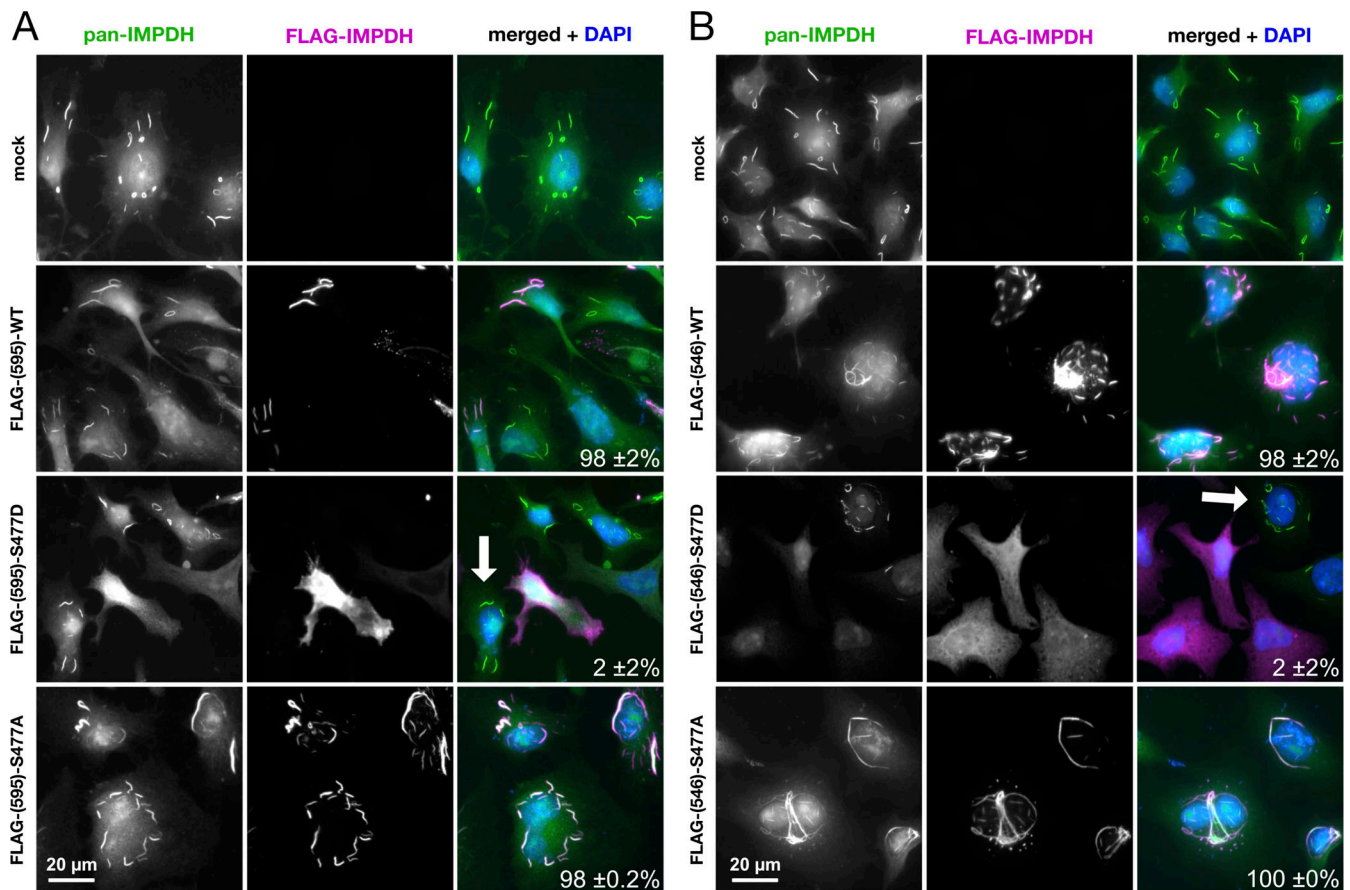
Figure 7. **S477D disrupts filament assembly in a dominant-negative manner in living cells. (A)** HeLa cells were transfected with FLAG-tagged IMPDH1(595)-WT, IMPDH1(595)-S477D, or IMPDH1(595)-S477A, then treated with 1 mM ribavirin for 2 h to induce filament assembly. Mock transfection is shown as a control. Green: all IMPDH (endogenous + transfected). Magenta: FLAG-tagged fusion proteins. Blue: nuclei stained with DAPI. White arrow: non-transfected cell with filament formation, serving as an internal control. Percentage of transfected cells containing filaments is displayed in the bottom right corner of merged panels. **(B)** Same experiment as in panel A, but with FLAG-tagged IMPDH1(546)-WT, IMPDH1(546)-S477D, and IMPDH1(546)-S477A. Two biological replicates were performed.

inability to form filaments at all in cells implies that IMPDH filaments predominantly assemble using the large interface in vivo. Together, our data suggest that phosphorylation at S477 is a molecular mechanism for regulating flux through de novo GTP synthesis by controlling higher-order assembly of the pathway's rate-limiting enzyme.

Discussion

Despite the increasing interest in higher-order assembly of IMPDH, posttranslational modifications of the enzyme have received little attention. However, a recent phosphoproteomic analysis of bovine retinas adapted to light and dark states shed light on three novel phosphorylation sites in IMPDH1: T159/S160, S416, and S477 (Plana-Bonamaisó et al., 2020). The study focused mainly on light-dependent phosphorylation at T159/S160, which desensitizes IMPDH1 to GTP inhibition to boost GTP levels in support of phototransduction. On the other hand, phosphorylation at S477 was correlated with the dark, when less GTP production is needed (Plana-Bonamaisó et al., 2020). S477D seemed to have no effect on basal IMPDH1(546) activity in vitro,

suggesting that S477D might instead play a structural role in disrupting filament assembly.

Here, we showed that S477D resensitizes human retinal IMPDH1 variants to GTP inhibition and prevents filament assembly in living cells in a dominant-negative manner, which would lead to overall decrease in cellular GTP pools. Our data demonstrate a mechanism for control of IMPDH filament assembly dynamics and GTP production by phosphorylation at a single site. We propose that phosphorylation at S477 reduces the extent of IMPDH filaments in photoreceptor cells in the dark, leading to a global decrease in GTP levels when nucleotide turnover rate is reduced. In the light, an unknown phosphatase removes the modification, allowing filaments to reassemble and boost GTP levels to support cGMP signaling again (Fig. 8).

The S477D mutation in either the 546 or 595 variant has a dominant-negative effect on assembly of endogenous WT IMPDH. IMPDH2 is the dominant isoform in most cell types and only assembles filaments via the large interface (Burrell et al., 2022; Johnson and Kollman, 2020). The dominant effect of IMPDH1(595)-S477D can be explained by its incorporation into mixed tetramers or octamers with the WT enzyme. Given our
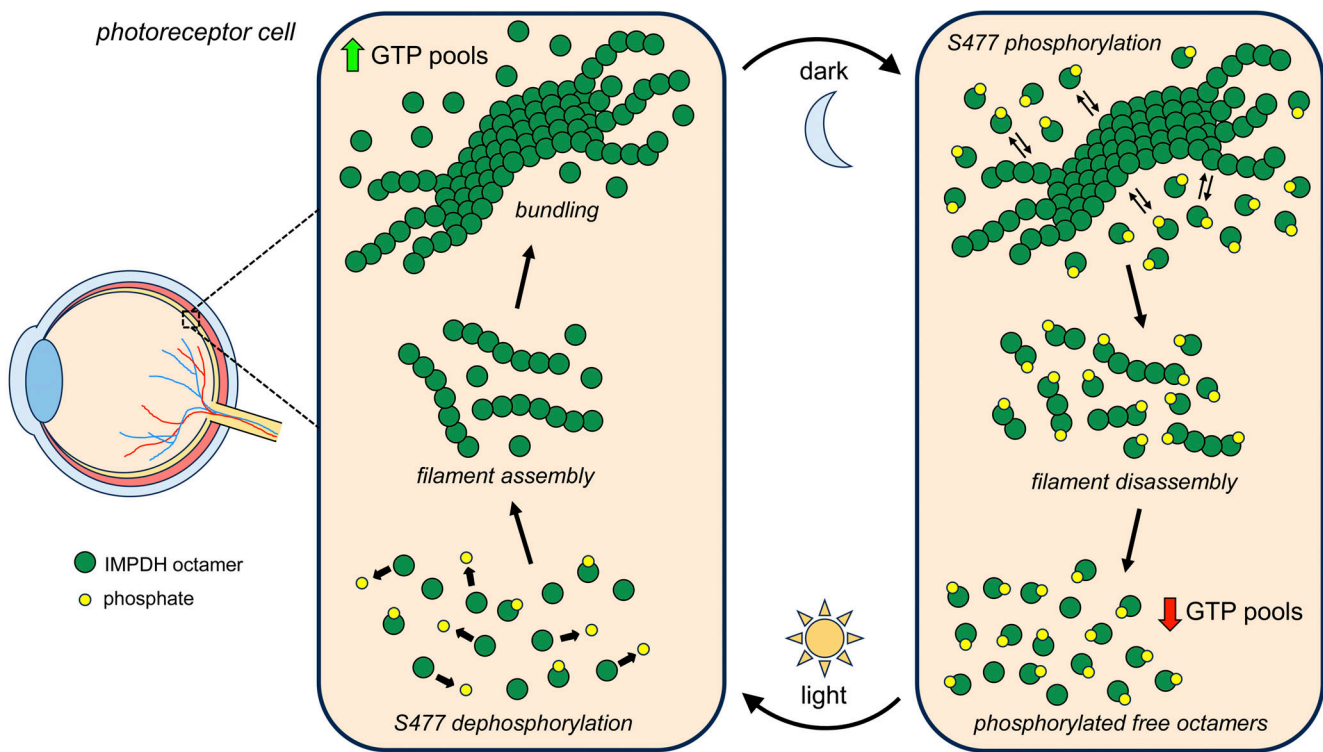
Figure 8. **Model of IMPDH1-S477 phosphorylation in the retina.** In the dark, phosphorylation of IMPDH1 at S477 disassembles filaments and the cellular pool of IMPDH shifts toward phosphorylated free octamers, leading to a decrease in GTP pools when less nucleotide turnover is occurring. In the light, S477 is dephosphorylated and filaments reassemble to boost GTP production when nucleotide turnover is higher. The cycle of IMPDH1 filament assembly and disassembly in light and dark states continues to regulate cellular GTP levels.

in vitro data that IMPDH1(546)-S477D assembles filaments in both active and inhibited states, we were initially surprised that it failed to form filaments at all in cells. However, this may again be explained by the likely coassembly of IMPDH1(546)-S477D into mixed oligomers with endogenous IMPDH (Keppeke et al., 2023). Mixed oligomers of IMPDH2 (large interface only) and IMPDH1(546)-S477D (small interface only) would prevent assembly of either filament type and likely explain the dominant-negative effect of IMPDH1(546)-S477D. It is possible that IMPDH1 assembles short filaments in cells using the small interface, but the incompatibility with IMPDH2 would render them short-lived. In the retina, which does not express appreciable levels of IMPDH2 or canonical IMPDH1 (Aherne et al., 2004; Bowne et al., 2006a; Hedstrom, 2009; Spellicy et al., 2007), mixed oligomers of WT IMPDH1(595) (large interface only) and WT IMPDH1(546) (small or large interface) would likely only assemble filaments with the large interface. Overall, this is consistent with the observation that IMPDH filaments form in cells and tissues under conditions of high demand for IMPDH activity (Calise et al., 2018; Chang et al., 2015; Duong-Ly et al., 2018; Keppeke et al., 2018, 2020; Peng et al., 2021; Ruan et al., 2020), which is promoted by assembly into filaments with the large interface. Further studies in genome-edited cells expressing single IMPDH variants will provide insight into in vivo assembly of the different forms of IMPDH.

We recently characterized IMPDH1 filaments in the zebrafish retina, finding a circadian pattern to filament assembly, with

elongated filaments forming in photoreceptors during the day and smaller punctate structures at night (Cleghorn et al., 2022). We also showed that the zebrafish IMPDH1 retinal variants are very similar to human IMPDH1 in terms of structure, filament assembly, and regulation (Cleghorn et al., 2022). This is consistent with our finding here that the S477D mutation, which mimics dark-dependent phosphorylation, disrupts filament assembly and reduces enzyme activity in the presence of GTP. Besides zebrafish, IMPDH filament assembly has also been observed in mouse retinas, although the functional significance is yet to be described (Fernández-Justel et al., 2019).

Studies in cultured cells and mice have demonstrated a strong link between IMPDH filament assembly and cells that consume high levels of GTP. Robust IMPDH filament assembly occurs in stem cells (Carcamo et al., 2011; Keppeke et al., 2018) and lymphocytes (Calise et al., 2018; Duong-Ly et al., 2018; Peng et al., 2021), which require increased nucleotides to support rapid proliferation (Dayton et al., 1994; Fairbanks et al., 1995; Quéméneur et al., 2003). IMPDH filaments have also been identified in aggressive tumors (Keppeke et al., 2020; Ruan et al., 2020). Polymerization of IMPDH1(546), IMPDH1(595), and IMPDH2 partially prevents feedback inhibition by guanine nucleotides compared with the unpolymerized state (Burrell et al., 2022; Fernández-Justel et al., 2019; Johnson and Kollman, 2020). In cells, this would allow accumulation of GTP to higher steady state levels, supporting rapid proliferation (IMPDH2) or phototransduction in photoreceptor cells (IMPDH1 retinal variants).

More than 20 different metabolic enzymes form filaments in cells, suggesting that filament assembly is a general mechanism for regulating multiple metabolic pathways (Hvorecny and Kollman, 2023; Lynch et al., 2020; Narayanaswamy et al., 2009; Noree et al., 2010; Park and Horton, 2019, 2020; Shen et al., 2016; Simonet et al., 2020). For many metabolic enzymes, filament formation is an important mechanism for fine-tuning catalytic activity (Barry et al., 2014; Hansen et al., 2021; Hu et al., 2022; Hunkeler et al., 2018; Hvorecny et al., 2023; Lu et al., 2023; Lynch and Kollman, 2020; Lynch et al., 2017; Polley et al., 2019; Stoddard et al., 2020; Zhong et al., 2022). Here, we demonstrate that filament assembly itself can be directly tuned by phosphorylation, adding an additional layer to an already complex mode of regulation for IMPDH that occurs at different levels. Activity of IMPDH tetramers is modulated by feedback inhibition and oligomerization into octamers. IMPDH octamers are then regulated further by allosteric binding of nucleotides to the Bateman domain, which compresses or extends the conformation of the octamer. Polymerization of octamers into filaments can then modulate sensitivity to GTP inhibition. Filament assembly itself is then regulated by phosphorylation at S477 in response to changing metabolic conditions of the cell.

IMPDH localizes to the purinosome (Zhao et al., 2015), a biomolecular condensate assembled by the six enzymes directly upstream of IMPDH in de novo purine synthesis (An et al., 2008; Pedley et al., 2022b). Purinosome assembly correlates with increased flux through the pathway (Pareek et al., 2020; Zhao et al., 2015) and has been hypothesized to be regulated by posttranslational modifications (Liu et al., 2019). In fact, purinosome assembly is modulated by casein kinase II, AMP-activated protein kinase, and 3-phosphoinositide–dependent protein kinase 1, suggesting various signaling cascades spatially regulate purinosome enzymes (An et al., 2010; Schmitt et al., 2016, 2018). It is enticing to speculate that a network of phosphorylation and/or other modifications may spatiotemporally coordinate assembly of IMPDH into various subcellular compartments depending on the metabolic state of the cell.

Given the widespread utilization of filament assembly as a regulatory mechanism, it is likely that other polymerizing enzymes are regulated by posttranslational modification in the same way. Some correlations between posttranslational modification and IMPDH or cytidine triphosphate synthetase (CTPS) filament assembly in cells have been reported. Ankyrin repeat domain-containing protein 9 (ANKRD9) is a component of a cullin-RING superfamily E3 ligase complex that ubiquitinates both isoforms of IMPDH for degradation (Lee et al., 2018). ANKRD9 also localizes to and stabilizes IMPDH filaments induced by serum starvation in HeLa cells, suggesting ubiquitination plays some role in filament assembly (Hayward et al., 2019). The E3 ubiquitin ligase activity of Cbl is required for CTPS filament assembly in Drosophila, although it is not clear if the ubiquitination is direct (Wang et al., 2015). In a similar fashion, protein methylation is required for CTPS filament assembly in human cells (Lin et al., 2018). The mechanisms underlying these modifications remain unclear, but our current study opens the possibility for direct posttranslational modification as a general mechanism for modulating filament assembly dynamics.

The data presented here establish a molecular mechanism for reversible phosphorylation controlling assembly of IMPDH filaments and regulating GTP levels in the retina. This mechanism is likely to apply to a variety of filament-forming enzymes coordinating many different metabolic pathways in the cell. Future studies will determine if phosphorylation or other posttranslational modifications are the mechanisms of control underlying general metabolic filament assembly in vivo.

Materials and methods

Molecular cloning

Kanamycin-resistant pSMT3 bacterial expression vectors containing coding sequences for human IMPDH1(546) and IMPDH1(595) with N-terminal 6xHis-SUMO tags were generated previously (Burrell et al., 2022). To generate S477D mutant versions, overlapping primers 5′-CGCAGCCTGGATGTCCTTCGGTCCA-3′ and 5′-TGGACCGAAGGACATCCAGGCTGCG-3′ containing a TC > GA change to replace a serine with an aspartic acid codon were used to amplify each plasmid. Plasmids were ligated at 50°C for 1 h in a Gibson assembly reaction. The reaction product was treated with DpnI enzyme at 37°C for 30 min to degrade template DNA and then used for transformation of competent TOP10 E. coli cells. Transformed cells were cultured overnight on lysogeny broth (LB) agar plates containing 50 µg/ml kanamycin. Single colonies were picked and cultured overnight in LB medium + 50 µg/ml kanamycin, and recombinant plasmids were isolated using the GeneJET Plasmid Miniprep Kit (#K0503; Thermo Fisher Scientific). Insert sequences in each plasmid were confirmed by Sanger sequencing. Vector sequence was previously confirmed by Sanger sequencing of parental constructs.

For mammalian expression, coding sequences for WT and S477D retinal variants were subcloned from the above constructs into a pCMV3 vector (generously provided by Dr. Gerson Keppeke, Universidad Católica del Norte, Coquimbo, Chile). S477D constructs were then used as templates for PCR reactions to generate full-length S477A constructs, which were then self-ligated by Gibson assembly. Primers used for cloning are listed in Table 2. The same procedure was used for cloning mammalian constructs as bacterial expression constructs (see above), except that different primers were used. Full-length plasmid sequencing was performed on all mammalian constructs by Nanopore sequencing. Insert regions were also validated by Sanger sequencing.

Recombinant IMPDH1 expression and purification

Recombinant human IMPDH1 retinal variant proteins were expressed and purified as described previously (Anthony et al., 2017; Burrell et al., 2022; Cleghorn et al., 2022). Briefly, BL21 (DE3) E. coli cells were transformed with WT or S477D mutant IMPDH1(546) or IMPDH1(595) expression vectors. Cells were cultured in LB medium at 37°C until reaching an optical density (OD$_{600}$) of 0.9, and then expression was induced by addition of isopropyl-β-d-thiogalactoside (IPTG) to 1 mM for 4 h at 30°C.

Calise et al.
Phosphorylation controls IMPDH1 filament assembly

Journal of Cell Biology 10 of 17
https://doi.org/10.1083/jcb.202310139

Table 2. **Primers used for cloning by Gibson assembly**

Construct	Insert forward primer (5′ → 3′)	Insert reverse primer (5′ → 3′)	Vector forward primer (5′ → 3′)	Vector reverse primer (5′ → 3′)
pCMV3_FLAG-IMPDH1(546)-WT	GACTACAAAGACGATGACGACAAGAGCATGGCGGACTACCTGATC	GAGGCTGATCAGCGGGTTTAATTATGCAGCGACGCAGTC	GACTGCGTCGCTGCATAATTAAACCCGCTGATCAGCC	CTGATCAGGTAGTCCGCCATGCTCTTGTCGTCATCG
pCMV3_FLAG-IMPDH1(546)-S477D	GACTACAAAGACGATGACGACAAGAGCATGGCGGACTACCTGATC	GAGGCTGATCAGCGGGTTTAATTATGCAGCGACGCAGTC	GACTGCGTCGCTGCATAATTAAACCCGCTGATCAGCC	CTGATCAGGTAGTCCGCCATGCTCTTGTCGTCATCG
pCMV3_FLAG-IMPDH1(595)-WT	GATGACGACAAGAGCATGGAGGGGCCACTCACTC	GAGGCTGATCAGCGGGTTTAATTATGCAGCGACGCAGTC	GACTGCGTCGCTGCATAATTAAACCCGCTGATCAGCC	GAGTGAGTGGCCCCTCCATGCTCTTGTCGTCATC
pCMV3_FLAG-IMPDH1(595)-S477D	GATGACGACAAGAGCATGGAGGGGCCACTCACTC	GAGGCTGATCAGCGGGTTTAATTATGCAGCGACGCAGTC	GACTGCGTCGCTGCATAATTAAACCCGCTGATCAGCC	GAGTGAGTGGCCCCTCCATGCTCTTGTCGTCATC
pCMV3_FLAG-IMPDH1(546)-S477A	CGCAGCCTGGCTGTCCTTCGGTCCATGATG	TGGACCGAAGGACAGCCAGGCTGCG		
pCMV3_FLAG-IMPDH1(595)-S477A	CGCAGCCTGGCTGTCCTTCGGTCCATGATG	TGGACCGAAGGACAGCCAGGCTGCG		

Cells were pelleted and flash-frozen in liquid nitrogen and stored at −80°C until use.

Pellets were thawed, resuspended in lysis buffer (50 mM KPO₄, 300 mM KCl, 10 mM imidazole, 800 mM urea, pH 8.0), and lysed with an Emulsiflex-05 homogenizer. Lysate was clarified by centrifugation at 33,746 × g for 30 min at 4°C and 6xHis-SUMO-tagged IMPDH1 was purified by immobilized metal ion affinity chromatography using HisTrap FF nickel sepharose columns (Cytiva) on an ÄKTA Start chromatography system. After on-column washing with lysis buffer, protein was eluted in buffer (50 mM KPO₄, 300 mM KCl, 500 mM imidazole, pH 8.0) and fractionated into 1-ml volumes. Peak fractions were combined and incubated with 1 mg ULP1 protease (Malakhov et al., 2004) per 100 mg IMPDH1 for 1 h on ice, then supplemented with 1 mM dithiothreitol (DTT) and 800 mM urea. Protein was concentrated with a 30,000 molecular weight cutoff filter (Amicon) and size-exclusion chromatography was performed on an ÄKTA Pure chromatography system using a Superose 6 column (Cytiva) pre-equilibrated in gel filtration buffer (20 mM HEPES, 100 mM KCl, 800 mM urea, 1 mM DTT, pH 8.0). Peak fractions were concentrated using a 10,000 molecular weight cutoff filter and then flash-frozen in liquid nitrogen and stored at −80°C.

Recombinant human IMPDH1(514) WT and S477D proteins were purified as described previously (Plana-Bonamaisó et al., 2020; Thomas et al., 2012). Briefly, BL21 (DE3) *E. coli* cells were transformed with pETEV15b constructs (Alonso-García et al., 2009) and expression was induced at 16°C for 12–14 h with 1 mM IPTG. Cell pellets were resuspended in 20 ml binding buffer (20 mM Tris, pH 8.0, 500 mM KCl, 20 mM imidazole, 1.5 M urea, and 1 mM DTT) containing protease inhibitors (Pierce protease inhibitor tablets, EDTA-free) per liter of cell culture. Lysates were sonicated on ice (8 W power, cycles of 30 s on and 30 s off) and then clarified at 17,000 × g for 30 min at 4°C. His-tagged IMPDH1 proteins were purified immediately after centrifugation by immobilized metal ion affinity chromatography on a HisTrap crude affinity resin (GE Healthcare) according to the manufacturer's instructions. Protein was eluted with binding buffer containing 500 mM imidazole and the His tag was cleaved overnight at room temperature (RT) with recombinant tobacco etch virus protease (0.2 mg per liter of culture) purified in-house while dialyzing against storage buffer (20 mM Tris, pH 8.0, 500 mM KCl, and 1 mM DTT). Cleaved proteins were concentrated and injected into a Sephacryl S300 HR 16/60 column (GE Healthcare) equilibrated in storage buffer. Protein fractions were concentrated, glycerol was added up to 10%, and aliquots were frozen at −80°C until use.

IMPDH1 activity assays

Aliquots of IMPDH1 protein were diluted at least 100-fold from gel filtration buffer (20 mM HEPES, 100 mM KCl, 800 mM urea, 1 mM DTT, pH 8.0) into activity buffer (20 mM HEPES, 100 mM KCl, 1 mM DTT, pH 7.0) to 1 µM concentration and incubated with 1 mM ATP, 1 mM IMP, 1 mM MgCl₂, and varying concentrations of GTP for 30 min at 20°C in 96-well ultraviolet transparent plates (#3679; Corning). 100 µl reactions were initiated by addition of 300 µM NAD⁺. NADH production was measured by optical absorbance at 340 nm at 25°C once per minute for 15 min with a Varioskan Lux microplate reader (Thermo Fisher Scientific). Absorbance was correlated with NADH concentration using a standard curve. Specific activity was calculated by linear interpretation of the reaction slope for a 5-min window beginning 2 min after reaction initiation. All data points are an average of three measurements from the same protein preparation. Error bars represent SD. Fits for activity assays were calculated in GraphPad Prism v10.1.1 using a variable slope four-parameter model with equation $V = V_{min} + (V_{max} - V_{min})/(1 + (IC_{50}/[I])^n)$ where n = Hill coefficient. Fitting method used was least squares regression and no weighting or constraints were applied. Confidence intervals were computed using the likelihood ratio asymmetric method. The IC₅₀ and Hill coefficient best-fit values and 90% confidence intervals are reported in Table 1.

Negative stain EM

Protein samples were diluted at least 100-fold from gel filtration buffer (20 mM HEPES, 100 mM KCl, 800 mM urea, 1 mM DTT, pH 8.0) into assembly buffer (20 mM HEPES, 100 mM KCl, 1 mM DTT, pH 7.0) to 1 µM concentration, and 2.5 µl volume was

Calise et al.
Phosphorylation controls IMPDH1 filament assembly

Journal of Cell Biology   11 of 17
https://doi.org/10.1083/jcb.202310139

applied to glow-discharged continuous carbon EM grids (Protochips) and stained with 0.7% uranyl formate as described previously (Johnson and Kollman, 2020). Grids were imaged by transmission EM at 100 kV accelerating voltage on an FEI Morgagni microscope equipped with a Gatan Orius CCD. Micrographs were collected at a nominal 22,000× magnification with a 3.9 Å pixel size.

Cryo-EM sample preparation and data collection
Protein samples were diluted from 20- to 100-fold from gel filtration buffer (20 mM HEPES, 100 mM KCl, 800 mM urea, 1 mM DTT, pH 8.0) into assembly buffer (20 mM HEPES, 100 mM KCl, 1 mM DTT, pH 7.0) to 1–5 µM concentration, and 2.5 µl volume was applied to glow-discharged C-flat holey carbon EM grids (Protochips), blotted at 4°C with 100% relative humidity, and plunge-frozen in liquid ethane using a Vitrobot vitrification system (Thermo Fisher Scientific) as described previously (Johnson and Kollman, 2020). High-throughput data collection was performed with Leginon (Suloway et al., 2009) or SerialEM (Mastronarde, 2005) software packages controlling a Thermo Fisher Scientific Glacios TEM operating at 200 kV equipped with a Gatan K2 Summit direct electron detector or a Thermo Fisher Scientific Titan Krios G3 TEM at 300 kV equipped with a Gatan image filter and K3 Summit direct electron detector.

Cryo-EM image processing
Movies were collected in super-resolution mode, then aligned and corrected for full-frame motion and sample deformation using the patch motion correction algorithm in CryoSPARC Live with 2× Fourier binning and dose compensation applied during motion correction (Punjani et al., 2017). Contrast transfer function (CTF) estimation, initial particle picking, and two-dimensional (2D) classification were performed in CryoSPARC Live. CryoSPARC v3 or v4 was used for all subsequent image processing. Each dataset was processed individually using a similar workflow.

After several rounds of 2D classification to select the best-resolved classes, particles were boxed and re-extracted to generate a quality particle stack for further processing. Either ab initio reconstruction was used to generate an initial volume from these particles or a map from a previous IMPDH filament structure lowpass-filtered to 30 Å was used as a starting volume for refinement. The D4 point-group symmetry of IMPDH filaments means there are two points along the filament that can be used as symmetry origins: the center of an octamer or at the assembly interface between octamers. Octamer-centered reconstructions of filaments were done with homogeneous or nonuniform refinement with D4 symmetry, per-particle defocus refinement, and per-group CTF refinement with a previously solved octamer-centered filament map (either extended or compressed) as the starting volume (Punjani et al., 2020). Interface-centered reconstructions were performed the same, except with a previously solved interface-centered filament map as a starting volume. Image processing workflows are provided for each structure (Figs. S2, S3, and S4). Directional Fourier shell correlation (FSC) was calculated using the remote 3DFSC processing server (https://3dfsc.salk.edu) (Tan et al., 2017).

Model building and refinement
Existing structures were used as templates for model building. Octamer-centered compressed IMPDH1(595)-WT (PDB: 7RGD) was a template for the IMPDH1(595)-S477D model. Octamer-centered compressed IMPDH1(546)-WT (PDB: 7RGQ), interface-centered compressed IMPDH1(546)-WT (PDB: 7RGI), octamer-centered extended IMPDH1(546)-WT (PDB: 7RGM), and interface-centered extended IMPDH1(546)-WT (PDB: 7RGL) were used as templates for IMPDH1(546)-S477D models. Initial templates were placed into cryo-EM densities by rigid-body fitting in UCSF ChimeraX v1.6.1 (Goddard et al., 2018). Then, initial models were examined and manually fit residue-by-residue using ISOLDE v1.6.0 (Croll, 2018). Manually adjusted models were then passed through real-space refinement in Phenix v1.20.1-4487 (Liebschner et al., 2019), and this process of manual and automated fitting was iterated several times to improve metrics like clash score, rotamer outliers, and Ramachandran outliers. Final models were then submitted through the PDB validation service, and remaining erroneous residues and ligands were manually adjusted in Coot v0.9.8.8 (Emsley et al., 2010) to generate deposited models. Fits of deposited models were consistent with the resolution of the maps. Data collection parameters and refinement statistics are summarized in Table 3. Figures were prepared with UCSF ChimeraX v1.6.1.

Human cell culture and transfection
HeLa cells (human cervical adenocarcinoma) were acquired from ATCC (#CCL-2) and maintained in DMEM medium (#10569010; Gibco) supplemented with 10% fetal bovine serum (#10437028; Gibco) in a 37°C incubator set to 5% atmospheric CO_2. Cells were subcultured 2–3 times per week with subcultivation ratios between 1:4 and 1:8 to maintain 50–80% confluence.

For transfection, HeLa cells were seeded at a density of 4×10^4 cells per well in 8-well chambered glass culture slides (#229168; Celltreat) and incubated overnight. The next day, culture medium was replaced with 345 µl fresh DMEM per well and mammalian expression plasmids were transfected into cells using the TransIT-HeLaMONSTER Transfection Kit (#MIR2904; Mirus Bio) according to the manufacturer's protocol. Briefly, transfections were prepared for each well as follows: 328 ng plasmid was mixed with 34 µl of Opti-MEM I Reduced Serum Medium (#31985070; Thermo Fisher Scientific) prior to the addition of 1 µl TransIT-HeLa Reagent, gentle mixing, and then addition of 0.67 µl MONSTER Reagent and further mixing. This transfection mixture was incubated for 20 min at RT prior to dropwise addition to the appropriate well. Cells were incubated for 48 h without media change, then treated (or not) with 1 mM ribavirin (#R9644; Sigma-Aldrich) for 2 h to induce filament assembly prior to fixation and immunofluorescence staining.

Indirect immunofluorescence
HeLa cells were fixed with 4% paraformaldehyde for 15 min at RT, washed 3× with PBS, then permeabilized with 0.1% Triton X-100 for 5 min at RT. Cells were washed 3× with PBS between all further steps. Cells were incubated with primary antibodies diluted in PBS for 1 h at RT, then with secondary antibodies

Table 3. Cryo-EM data collection, refinement, and validation statistics

	IMPDH1(595)-S477D compressed free octamer	IMPDH1(546)-S477D compressed filament octamer	IMPDH1(546)-S477D compressed filament interface	IMPDH1(546)-S477D extended filament octamer	IMPDH1(546)-S477D extended filament interface
Ligands	GTP, ATP, IMP, NAD⁺	GTP, ATP, IMP, NAD⁺	GTP, ATP, IMP, NAD⁺	ATP, IMP, NAD⁺	ATP, IMP, NAD⁺
PDB ID	8U7M	8U7Q	8U7V	8U8O	8U8Y
EMDB ID	EMD-41986	EMD-41989	EMD-42012	EMD-42026	EMD-42029
Data collection and refinement					
Magnification	36,000	36,000	36,000	105,000	105,000
Voltage (kV)	200	200	200	300	300
Electron exposure (e⁻/Å²)	65	50	50	50	50
Defocus range (µm)	−1.8 to −1.2	−1.8 to −1.2	−1.8 to −1.2	−1.8 to −1.2	−1.8 to −1.2
Pixel size (data collection) (Å)	1.16	1.16	1.16	0.4215	0.4215
Pixel size (reconstruction) (Å)	1.16	1.16	1.16	0.843	0.843
Micrographs (no.)	646	756	756	4,632	4,632
Initial particles (no.)	343,619	434,369	434,369	5,836,476	5,836,476
Final particles (no.)	163,814	163,916	149,184	1,773,701	1,951,413
Symmetry imposed	D4	D4	D4	D4	D4
Resolution (CryoSPARC) postprocess (0.143 FSC) (Å)	3.1	3.3	3.3	2.4	2.1
Resolution (3DFSC) (0.5 FSC_ref) (Å)	3.2	3.4	3.5	2.4	2.3
Model refinement and validation					
Initial model (PDB ID)	7RGD	7RGQ	7RGI	7RGM	7RGL
Root-mean-square deviations					
Bond lengths (Å)	0.017	0.017	0.017	0.014	0.011
Bond angles (°)	1.378	1.334	1.412	1.302	0.989
MolProbity score	1.79	1.60	1.66	1.44	1.30
Clash score	10.32	6.75	7.94	3.62	2.24
C-β deviations	0%	0%	0%	0%	0%
Rotamer outliers (%)	0.27%	0.73%	0.85%	1.24%	1.76%
Ramachandran plot					
Favored (%)	96.23%	96.51%	96.52%	96.64%	97.44%
Allowed (%)	3.77%	3.28%	3.27%	3.36%	2.56%
Disallowed (%)	0%	0.21%	0.22%	0%	0%
Cross-correlation (mask)	0.69	0.83	0.83	0.75	0.86
Map resolution estimates					
FSC 0.5 (masked)	3.63	3.45	3.50	2.54	2.13
FSC 0.5 (unmasked)	3.64	3.56	3.72	2.63	2.26

diluted in PBS for 1 h at RT in the dark, and finally with 5 µM DAPI (ab228549; Abcam) in PBS for 20 min at RT in the dark. The slide was mounted with ProLong Glass Antifade Mountant (#P36984; Thermo Fisher Scientific) on #1.5 thickness cover-glass (#48393-251; VWR) and allowed to cure for 24 h prior to imaging. Slides were imaged at RT on a Leica DM5500B widefield fluorescence microscope equiped with a Leica HCX PL Fluotar 40X 0.75 numerical aperture objective, Lumencor SOLA Light Engine solid-state light source, Leica DAPI ET, GFP ET, and TXR ET filters, and Hamamatsu ORCA-Flash 4.0 LT sCMOS camera controlled by Leica Application Suite X acquisition software. Composite images were generated from single-channel micrographs using Fiji/ImageJ v1.54f (Schindelin et al., 2012).

Primary antibodies used were rabbit polyclonal IgG anti-IMPDH2 (1:500, #12948-1-AP; Proteintech) and mouse monoclonal IgG1 anti-FLAG epitope tag (1:200, #66008-3-Ig; Proteintech). Secondary antibodies used were Alexa Fluor 488-conjugated goat anti-rabbit IgG (1:400, #ab150077; Abcam) and Alexa Fluor 594-conjugated goat anti-mouse IgG (1:400, #ab150120; Abcam).

For quantification of the percentage of cells containing filaments (Figs. 7 and S5), two biological replicates were performed and a minimum of 100 cells were counted in each transfection condition.

Online supplemental material
Fig. S1 demonstrates by negative stain EM that S477D partially disrupts filament assembly of the canonical IMPDH1(514) under the same assay conditions as the retinal variants. Figs. S2, S3, and S4 summarize the cryo-EM data processing workflows for the inhibited IMPDH1(595)-S477D, inhibited IMPDH1(546)-S477D, and active IMPDH1(546)-S477D structures, respectively. They also contain example micrographs, 2D classes, FSC curves, and densities for bound ligands. Fig. S5 shows the same experiment as Fig. 7 but without ribavirin treatment, as overexpression of IMPDH1 alone leads to filament assembly.

Data availability
Coordinates for atomic models are deposited in the PDB with accession codes: compressed IMPDH1(595)-S477D free octamer (8U7M); compressed IMPDH1(546)-S477D filament, octamer-centered (8U7Q); compressed IMPDH1(546)-S477D filament, interface-centered (8U7V); extended IMPDH1(546)-S477D filament, octamer-centered (8U8O); and extended IMPDH1(546)-S477D filament, interface-centered (8U8Y). Cryo-EM maps are deposited in the Electron Microscopy Data Bank with accession codes: compressed IMPDH1(595)-S477D free octamer (EMD-41986); compressed IMPDH1(546)-S477D filament, octamer-centered (EMD-41989); compressed IMPDH1(546)-S477D filament, interface-centered (EMD-42012); extended IMPDH1(546)-S477D filament, octamer-centered (EMD-42026); and extended IMPDH1(546)-S477D filament, interface-centered (EMD-42029).

Acknowledgments
The authors would like to thank the Arnold and Mabel Beckman Cryo-EM Center at the University of Washington for access to electron microscopes. We also thank Alex Merz for the use of a biosafety cabinet and incubators for human cell culture; Suzanne Hoppins and Andrea Wills for fluorescence microscope use; and Kelli Hvorecny, Eric Lynch, Richard Muniz, and Lauren Salay for fruitful discussion.

References

Aherne, A., A. Kennan, P.F. Kenna, N. McNally, D.G. Lloyd, I.L. Alberts, A.-S. Kiang, M.M. Humphries, C. Ayuso, P.C. Engel, et al. 2004. On the molecular pathology of neurodegeneration in IMPDH1-based retinitis pigmentosa. *Hum. Mol. Genet.* 13:641–650. https://doi.org/10.1093/hmg/ddh061

Alonso-García, N., A. Inglés-Prieto, A. Sonnenberg, and J.M. de Pereda. 2009. Structure of the Calx-beta domain of the integrin beta4 subunit: Insights into function and cation-independent stability. *Acta Crystallogr. D Biol. Crystallogr.* 65:858–871. https://doi.org/10.1107/S0907444909018745

An, S., R. Kumar, E.D. Sheets, and S.J. Benkovic. 2008. Reversible compartmentalization of de novo purine biosynthetic complexes in living cells. *Science.* 320:103–106. https://doi.org/10.1126/science.1152241

An, S., M. Kyoung, J.J. Allen, K.M. Shokat, and S.J. Benkovic. 2010. Dynamic regulation of a metabolic multi-enzyme complex by protein kinase CK2. *J. Biol. Chem.* 285:11093–11099. https://doi.org/10.1074/jbc.M110.101139

Andashti, B., R. Yazdanparast, E. Barzegari, and H. Galehdari. 2020. The functional impact of the C/N-terminal extensions of the mouse retinal IMPDH1 isoforms: A kinetic evaluation. *Mol. Cell. Biochem.* 465:155–164. https://doi.org/10.1007/s11010-019-03675-9

Andashti, B., R. Yazdanparast, M. Motahar, E. Barzegari, and H. Galehdari. 2021. Terminal peptide extensions augment the retinal IMPDH1 catalytic activity and attenuate the ATP-induced fibrillation events. *Cell Biochem. Biophys.* 79:221–229. https://doi.org/10.1007/s12013-021-00973-2

Anthony, S.A., A.L. Burrell, M.C. Johnson, K.C. Duong-Ly, Y.-M. Kuo, J.C. Simonet, P. Michener, A. Andrews, J.M. Kollman, and J.R. Peterson. 2017. Reconstituted IMPDH polymers accommodate both catalytically active and inactive conformations. *Mol. Biol. Cell.* 28:2600–2608. https://doi.org/10.1091/mbc.e17-04-0263

Calise et al.
Phosphorylation controls IMPDH1 filament assembly

Journal of Cell Biology   14 of 17
https://doi.org/10.1083/jcb.202310139

![JCB logo]

Barry, R.M., A.-F. Bitbol, A. Lorestani, E.J. Charles, C.H. Habrian, J.M. Hansen, H.-J. Li, E.P. Baldwin, N.S. Wingreen, J.M. Kollman, and Z. Gitai. 2014. Large-scale filament formation inhibits the activity of CTP synthetase. *Elife*. 3:e03638. https://doi.org/10.7554/eLife.03638

Bowne, S.J., Q. Liu, L.S. Sullivan, J. Zhu, C.J. Spellicy, C.B. Rickman, E.A. Pierce, and S.P. Daiger. 2006a. Why do mutations in the ubiquitously expressed housekeeping gene IMPDH1 cause retina-specific photoreceptor degeneration? *Invest. Ophthalmol. Vis. Sci.* 47:3754–3765. https://doi.org/10.1167/iovs.06-0207

Bowne, S.J., L.S. Sullivan, S.H. Blanton, C.L. Cepko, S. Blackshaw, D.G. Birch, D. Hughbanks-Wheaton, J.R. Heckenlively, and S.P. Daiger. 2002. Mutations in the inosine monophosphate dehydrogenase 1 gene (IMPDH1) cause the RP10 form of autosomal dominant retinitis pigmentosa. *Hum. Mol. Genet.* 11:559–568. https://doi.org/10.1093/hmg/11.5.559

Bowne, S.J., L.S. Sullivan, S.E. Mortimer, L. Hedstrom, J. Zhu, C.J. Spellicy, A.I. Gire, D. Hughbanks-Wheaton, D.G. Birch, R.A. Lewis, et al. 2006b. Spectrum and frequency of mutations in IMPDH1 associated with autosomal dominant retinitis pigmentosa and leber congenital amaurosis. *Invest. Ophthalmol. Vis. Sci.* 47:34–42. https://doi.org/10.1167/iovs.05-0868

Buey, R.M., D. Fernández-Justel, A. Jiménez, and J.L. Revuelta. 2022. The gateway to guanine nucleotides: Allosteric regulation of IMP dehydrogenases. *Protein Sci. Publ. Protein Soc.* 31:e4399. https://doi.org/10.1002/pro.4399

Buey, R.M., D. Fernández-Justel, Í. Marcos-Alcalde, G. Winter, P. Gómez-Puertas, J.M. de Pereda, and J. Luis Revuelta. 2017. A nucleotide-controlled conformational switch modulates the activity of eukaryotic IMP dehydrogenases. *Sci. Rep.* 7:2648. https://doi.org/10.1038/s41598-017-02805-x

Buey, R.M., R. Ledesma-Amaro, A. Velázquez-Campoy, M. Balsera, M. Chagoyen, J.M. de Pereda, and J.L. Revuelta. 2015. Guanine nucleotide binding to the bateman domain mediates the allosteric inhibition of eukaryotic IMP dehydrogenases. *Nat. Commun.* 6:8923. https://doi.org/10.1038/ncomms9923

Burrell, A.L., and J.M. Kollman. 2022. IMPDH dysregulation in disease: A mini review. *Biochem. Soc. Trans.* 50:71–82. https://doi.org/10.1042/BST20210446

Burrell, A.L., C. Nie, M. Said, J.C. Simonet, D. Fernández-Justel, M.C. Johnson, J. Quispe, R.M. Buey, J.R. Peterson, and J.M. Kollman. 2022. IMPDH1 retinal variants control filament architecture to tune allosteric regulation. *Nat. Struct. Mol. Biol.* 29:47–58. https://doi.org/10.1038/s41594-021-00706-2

Calise, S.J., G. Abboud, H. Kasahara, L. Morel, and E.K.L. Chan. 2018. Immune response-dependent assembly of IMP dehydrogenase filaments. *Front. Immunol.* 9:2789. https://doi.org/10.3389/fimmu.2018.02789

Calise, S.J., and E.K.L. Chan. 2020. Anti-rods/rings autoantibody and IMPDH filaments: An update after fifteen years of discovery. *Autoimmun. Rev.* 19:102643. https://doi.org/10.1016/j.autrev.2020.102643

Calise, S.J., D.L. Purich, T. Nguyen, D.A. Saleem, C. Krueger, J.D. Yin, and E.K.L. Chan. 2016. 'Rod and ring' formation from IMP dehydrogenase is regulated through the one-carbon metabolic pathway. *J. Cell Sci.* 129:3042–3052. https://doi.org/10.1242/jcs.183400

Carcamo, W.C., M. Satoh, H. Kasahara, N. Terada, T. Hamazaki, J.Y.F. Chan, B. Yao, S. Tamayo, G. Covini, C.A. von Mühlen, and E.K.L. Chan. 2011. Induction of cytoplasmic rods and rings structures by inhibition of the CTP and GTP synthetic pathway in mammalian cells. *PLoS One.* 6:e29690. https://doi.org/10.1371/journal.pone.0029690

Carr, S.F., E. Papp, J.C. Wu, and Y. Natsumeda. 1993. Characterization of human type I and type II IMP dehydrogenase. *J. Biol. Chem.* 268:27286–27290. https://doi.org/10.1016/S0021-9258(19)74247-1

Chang, C.-C., W.-C. Lin, L.-M. Pai, H.-S. Lee, S.-C. Wu, S.-T. Ding, J.-L. Liu, and L.-Y. Sung. 2015. Cytoophidium assembly reflects upregulation of IMPDH activity. *J. Cell Sci.* 128:3550–3555. https://doi.org/10.1242/jcs.175265

Cleghorn, W.M., A.L. Burrell, M.M. Giarmarco, D.C. Brock, Y. Wang, Z.S. Chambers, J. Du, J.M. Kollman, and S.E. Brockerhoff. 2022. A highly conserved zebrafish IMPDH retinal isoform produces the majority of guanine and forms dynamic protein filaments in photoreceptor cells. *J. Biol. Chem.* 298:101441. https://doi.org/10.1016/j.jbc.2021.101441

Collart, F.R., C.B. Chubb, B.L. Mirkin, and E. Huberman. 1992. Increased inosine-5′-phosphate dehydrogenase gene expression in solid tumor tissues and tumor cell lines. *Cancer Res.* 52:5826–5828. https://doi.org/10.2172/10148922

Covini, G., W.C. Carcamo, E. Bredi, C.A. von Mühlen, M. Colombo, and E.K.L. Chan. 2012. Cytoplasmic rods and rings autoantibodies developed during pegylated interferon and ribavirin therapy in patients with chronic hepatitis C. *Antivir. Ther.* 17:805–811. https://doi.org/10.3851/IMP1993

Croll, T.I. 2018. ISOLDE: A physically realistic environment for model building into low-resolution electron-density maps. *Acta Crystallogr. D Struct. Biol.* 74:519–530. https://doi.org/10.1107/S2059798318002425

Dayton, J.S., T. Lindsten, C.B. Thompson, and B.S. Mitchell. 1994. Effects of human T lymphocyte activation on inosine monophosphate dehydrogenase expression. *J. Immunol.* 152:984–991. https://doi.org/10.4049/jimmunol.152.3.984

Duong-Ly, K.C., Y.-M. Kuo, M.C. Johnson, J.M. Cote, J.M. Kollman, J. Soboloff, G.F. Rall, A.J. Andrews, and J.R. Peterson. 2018. T cell activation triggers reversible inosine-5′-monophosphate dehydrogenase assembly. *J. Cell Sci.* 131:jcs223289. https://doi.org/10.1242/jcs.223289

Emsley, P., B. Lohkamp, W.G. Scott, and K. Cowtan. 2010. Features and development of Coot. *Acta Crystallogr. D Biol. Crystallogr.* 66:486–501. https://doi.org/10.1107/S0907444910007493

Fairbanks, L.D., M. Bofill, K. Ruckemann, and H.A. Simmonds. 1995. Importance of ribonucleotide availability to proliferating T-lymphocytes from healthy humans. Disproportionate expansion of pyrimidine pools and contrasting effects of de novo synthesis inhibitors. *J. Biol. Chem.* 270:29682–29689. https://doi.org/10.1074/jbc.270.50.29682

Fernández-Justel, D., R. Núñez, J. Martín-Benito, D. Jimeno, A. González-López, E.M. Soriano, J.L. Revuelta, and R.M. Buey. 2019. A nucleotide-dependent conformational switch controls the polymerization of human IMP dehydrogenases to modulate their catalytic activity. *J. Mol. Biol.* 431:956–969. https://doi.org/10.1016/j.jmb.2019.01.020

Goddard, T.D., C.C. Huang, E.C. Meng, E.F. Pettersen, G.S. Couch, J.H. Morris, and T.E. Ferrin. 2018. UCSF ChimeraX: Meeting modern challenges in visualization and analysis. *Protein Sci. Publ. Protein Soc.* 27:14–25. https://doi.org/10.1002/pro.3235

Grover, S., G.A. Fishman, and E.M. Stone. 2004. A novel IMPDH1 mutation (Arg231Pro) in a family with a severe form of autosomal dominant retinitis pigmentosa. *Ophthalmology*. 111:1910–1916. https://doi.org/10.1016/j.ophtha.2004.03.039

Gunter, J.H., E.C. Thomas, N. Lengefeld, S.J. Kruger, L. Worton, E.M. Gardiner, A. Jones, N.L. Barnett, and J.P. Whitehead. 2008. Characterisation of inosine monophosphate dehydrogenase expression during retinal development: Differences between variants and isoforms. *Int. J. Biochem. Cell Biol.* 40:1716–1728. https://doi.org/10.1016/j.biocel.2007.12.018

Hansen, J.M., A. Horowitz, E.M. Lynch, D.P. Farrell, J. Quispe, F. DiMaio, and J.M. Kollman. 2021. Cryo-EM structures of CTP synthase filaments reveal mechanism of pH-sensitive assembly during budding yeast starvation. *Elife*. 10:e73368. https://doi.org/10.7554/eLife.73368

Hayward, D., V.L. Kouznetsova, H.E. Pierson, N.M. Hasan, E.R. Guzman, I.F. Tsigelny, and S. Lutsenko. 2019. ANKRD9 is a metabolically-controlled regulator of IMPDH2 abundance and macro-assembly. *J. Biol. Chem.* 294:14454–14466. https://doi.org/10.1074/jbc.RA119.008231

Hedstrom, L. 2009. IMP dehydrogenase: Structure, mechanism, and inhibition. *Chem. Rev.* 109:2903–2928. https://doi.org/10.1021/cr900021w

Hu, H.-H., G.-M. Lu, C.-C. Chang, Y. Li, J. Zhong, C.-J. Guo, X. Zhou, B. Yin, T. Zhang, and J.-L. Liu. 2022. Filamentation modulates allosteric regulation of PRPS. *Elife*. 11:e79552. https://doi.org/10.7554/eLife.79552

Hunkeler, M., A. Hagmann, E. Stuttfeld, M. Chami, Y. Guri, H. Stahlberg, and T. Maier. 2018. Structural basis for regulation of human acetyl-CoA carboxylase. *Nature*. 558:470–474. https://doi.org/10.1038/s41586-018-0201-4

Hvorecny, K.L., K. Hargett, J.D. Quispe, and J.M. Kollman. 2023. Human PRPS1 filaments stabilize allosteric sites to regulate activity. *Nat. Struct. Mol. Biol.* 30:391–402. https://doi.org/10.1038/s41594-023-00921-z

Hvorecny, K.L., and J.M. Kollman. 2023. Greater than the sum of parts: Mechanisms of metabolic regulation by enzyme filaments. *Curr. Opin. Struct. Biol.* 79:102530. https://doi.org/10.1016/j.sbi.2023.102530

Jackson, R.C., G. Weber, and H.P. Morris. 1975. IMP dehydrogenase, an enzyme linked with proliferation and malignancy. *Nature*. 256:331–333. https://doi.org/10.1038/256331a0

Johnson, M.C., and J.M. Kollman. 2020. Cryo-EM structures demonstrate human IMPDH2 filament assembly tunes allosteric regulation. *Elife*. 9:e53243. https://doi.org/10.7554/eLife.53243

Juda, P., J. Smigová, L. Kováčik, E. Bártová, and I. Raška. 2014. Ultrastructure of cytoplasmic and nuclear inosine-5′-monophosphate dehydrogenase 2 "rods and rings" inclusions. *J. Histochem. Cytochem. Off. J. Histochem. Soc.* 62:739–750. https://doi.org/10.1369/0022155414543853

Kennan, A., A. Aherne, A. Palfi, M. Humphries, A. McKee, A. Stitt, D.A.C. Simpson, K. Demtroder, T. Orntoft, C. Ayuso, et al. 2002. Identification

of an IMPDH1 mutation in autosomal dominant retinitis pigmentosa (RP10) revealed following comparative microarray analysis of transcripts derived from retinas of wild-type and Rho(−/−) mice. *Hum. Mol. Genet.* 11:547–557. https://doi.org/10.1093/hmg/11.5.547

Keppeke, G.D., D. Barcelos, M. Fernandes, A.N. Comodo, D.P. Guimarães, L. Cardili, F.C.L. Carapeto, L.E.C. Andrade, and G. Landman. 2020. IMP dehydrogenase rod/ring structures in acral melanomas. *Pigment Cell Melanoma Res.* 33:490–497. https://doi.org/10.1111/pcmr.12854

Keppeke, G.D., S.J. Calise, E.K.L. Chan, and L.E.C. Andrade. 2015. Assembly of IMPDH2-based, CTPS-based, and mixed rod/ring structures is dependent on cell type and conditions of induction. *J. Genet. Genomics.* 42:287–299. https://doi.org/10.1016/j.jgg.2015.04.002

Keppeke, G.D., C.C. Chang, M. Peng, L.-Y. Chen, W.-C. Lin, L.-M. Pai, L.E.C. Andrade, L.-Y. Sung, and J.-L. Liu. 2018. IMP/GTP balance modulates cytoophidium assembly and IMPDH activity. *Cell Div.* 13:5. https://doi.org/10.1186/s13008-018-0038-0

Keppeke, G.D., C.-C. Chang, Z. Zhang, and J.-L. Liu. 2023. Effect on cell survival and cytoophidium assembly of the adRP-10-related IMPDH1 missense mutation Asp226Asn. *Front. Cell Dev. Biol.* 11:1234592. https://doi.org/10.3389/fcell.2023.1234592

Lee, Y., B. Lim, S.W. Lee, W.R. Lee, Y.-I. Kim, M. Kim, H. Ju, M.Y. Kim, S.-J. Kang, J.-J. Song, et al. 2018. ANKRD9 is associated with tumor suppression as a substrate receptor subunit of ubiquitin ligase. *Biochim. Biophys. Acta Mol. Basis Dis.* 1864:3145–3153. https://doi.org/10.1016/j.bbadis.2018.07.001

Liebschner, D., P.V. Afonine, M.L. Baker, G. Bunkóczi, V.B. Chen, T.I. Croll, B. Hintze, L.W. Hung, S. Jain, A.J. McCoy, et al. 2019. Macromolecular structure determination using X-rays, neutrons and electrons: Recent developments in Phenix. *Acta Crystallogr. D Struct. Biol.* 75:861–877. https://doi.org/10.1107/S2059798319011471

Lin, W.-C., A. Chakraborty, S.-C. Huang, P.-Y. Wang, Y.-J. Hsieh, K.-Y. Chien, Y.-H. Lee, C.-C. Chang, H.-Y. Tang, Y.-T. Lin, et al. 2018. Histidine-dependent protein methylation is required for compartmentalization of CTP synthase. *Cell Rep.* 24:2733–2745.e7. https://doi.org/10.1016/j.celrep.2018.08.007

Liu, C., G.M. Knudsen, A.M. Pedley, J. He, J.L. Johnson, T.M. Yaron, L.C. Cantley, and S.J. Benkovic. 2019. Mapping post-translational modifications of de Novo purine biosynthetic enzymes: Implications for pathway regulation. *J. Proteome Res.* 18:2078–2087. https://doi.org/10.1021/acs.jproteome.8b00969

Lu, G.-M., H.-H. Hu, C.-C. Chang, J. Zhong, X. Zhou, C.-J. Guo, T. Zhang, Y.-L. Li, B. Yin, and J.-L. Liu. 2023. Structural basis of human PRPS2 filaments. *Cell Biosci.* 13:100. https://doi.org/10.1186/s13578-023-01037-z

Lynch, E.M., D.R. Hicks, M. Shepherd, J.A. Endrizzi, A. Maker, J.M. Hansen, R.M. Barry, Z. Gitai, E.P. Baldwin, and J.M. Kollman. 2017. Human CTP synthase filament structure reveals the active enzyme conformation. *Nat. Struct. Mol. Biol.* 24:507–514. https://doi.org/10.1038/nsmb.3407

Lynch, E.M., and J.M. Kollman. 2020. Coupled structural transitions enable highly cooperative regulation of human CTPS2 filaments. *Nat. Struct. Mol. Biol.* 27:42–48. https://doi.org/10.1038/s41594-019-0352-5

Lynch, E.M., J.M. Kollman, and B.A. Webb. 2020. Filament formation by metabolic enzymes-A new twist on regulation. *Curr. Opin. Cell Biol.* 66:28–33. https://doi.org/10.1016/j.ceb.2020.04.006

Malakhov, M.P., M.R. Mattern, O.A. Malakhova, M. Drinker, S.D. Weeks, and T.R. Butt. 2004. SUMO fusions and SUMO-specific protease for efficient expression and purification of proteins. *J. Struct. Funct. Genomics.* 5:75–86. https://doi.org/10.1023/B:JSFG.0000029237.70316.52

Mastronarde, D.N. 2005. Automated electron microscope tomography using robust prediction of specimen movements. *J. Struct. Biol.* 152:36–51. https://doi.org/10.1016/j.jsb.2005.07.007

Mortimer, S.E., and L. Hedstrom. 2005. Autosomal dominant retinitis pigmentosa mutations in inosine 5′-monophosphate dehydrogenase type I disrupt nucleic acid binding. *Biochem. J.* 390:41–47. https://doi.org/10.1042/BJ20042051

Nagai, M., Y. Natsumeda, and G. Weber. 1992. Proliferation-linked regulation of type II IMP dehydrogenase gene in human normal lymphocytes and HL-60 leukemic cells. *Cancer Res.* 52:258–261.

Narayanaswamy, R., M. Levy, M. Tschansky, G.M. Stovall, J.D. O'Connell, J. Mirrielees, A.D. Ellington, and E.M. Marcotte. 2009. Widespread reorganization of metabolic enzymes into reversible assemblies upon nutrient starvation. *Proc. Natl. Acad. Sci. USA.* 106:10147–10152. https://doi.org/10.1073/pnas.0812771106

Noree, C., B.K. Sato, R.M. Broyer, and J.E. Wilhelm. 2010. Identification of novel filament-forming proteins in *Saccharomyces cerevisiae* and *Drosophila melanogaster*. *J. Cell Biol.* 190:541–551. https://doi.org/10.1083/jcb.201003001

Pareek, V., H. Tian, N. Winograd, and S.J. Benkovic. 2020. Metabolomics and mass spectrometry imaging reveal channeled de novo purine synthesis in cells. *Science.* 368:283–290. https://doi.org/10.1126/science.aaz6465

Park, C.K., and N.C. Horton. 2019. Structures, functions, and mechanisms of filament forming enzymes: A renaissance of enzyme filamentation. *Biophys. Rev.* 11:927–994. https://doi.org/10.1007/s12551-019-00602-6

Park, C.K., and N.C. Horton. 2020. Novel insights into filament-forming enzymes. *Nat. Rev. Mol. Cell Biol.* 21:1–2. https://doi.org/10.1038/s41580-019-0188-1

Pedley, A.M., J.P. Boylan, C.Y. Chan, E.L. Kennedy, M. Kyoung, and S.J. Benkovic. 2022a. Purine biosynthetic enzymes assemble into liquid-like condensates dependent on the activity of chaperone protein HSP90. *J. Biol. Chem.* 298:101845. https://doi.org/10.1016/j.jbc.2022.101845

Pedley, A.M., V. Pareek, and S.J. Benkovic. 2022b. The purinosome: A case study for a mammalian metabolon. *Annu. Rev. Biochem.* 91:89–106. https://doi.org/10.1146/annurev-biochem-032620-105728

Peng, M., C.-C. Chang, J.-L. Liu, and L.-Y. Sung. 2021. CTPS and IMPDH form cytoophidia in developmental thymocytes. *Exp. Cell Res.* 405:112662. https://doi.org/10.1016/j.yexcr.2021.112662

Plana-Bonamaisó, A., S. López-Begines, D. Fernández-Justel, A. Junza, A. Soler-Tapia, J. Andilla, P. Loza-Alvarez, J.L. Rosa, E. Miralles, I. Casals, et al. 2020. Post-translational regulation of retinal IMPDH1 in vivo to adjust GTP synthesis to illumination conditions. *Elife.* 9:e56418. https://doi.org/10.7554/eLife.56418

Polley, S., D. Lyumkis, and N.C. Horton. 2019. Mechanism of filamentation-induced allosteric activation of the SgrAI endonuclease. *Structure.* 27:1497–1507.e3. https://doi.org/10.1016/j.str.2019.08.001

Punjani, A., J.L. Rubinstein, D.J. Fleet, and M.A. Brubaker. 2017. cryoSPARC: Algorithms for rapid unsupervised cryo-EM structure determination. *Nat. Methods.* 14:290–296. https://doi.org/10.1038/nmeth.4169

Punjani, A., H. Zhang, and D.J. Fleet. 2020. Non-uniform refinement: Adaptive regularization improves single-particle cryo-EM reconstruction. *Nat. Methods.* 17:1214–1221. https://doi.org/10.1038/s41592-020-00990-8

Quéméneur, L., L.-M. Gerland, M. Flacher, M. Ffrench, J.-P. Revillard, and L. Genestier. 2003. Differential control of cell cycle, proliferation, and survival of primary T lymphocytes by purine and pyrimidine nucleotides. *J. Immunol.* 170:4986–4995. https://doi.org/10.4049/jimmunol.170.10.4986

Ruan, H., Z. Song, Q. Cao, D. Ni, T. Xu, K. Wang, L. Bao, J. Tong, H. Xiao, W. Xiao, et al. 2020. IMPDH1/YB-1 positive feedback loop assembles cytoophidia and represents a therapeutic target in metastatic tumors. *Mol. Ther.* 28:1299–1313. https://doi.org/10.1016/j.ymthe.2020.03.001

Schiavon, C.R., M.E. Griffin, M. Pirozzi, R. Parashuraman, W. Zhou, H.A. Jinnah, D. Reines, and R.A. Kahn. 2018. Compositional complexity of rods and rings. *Mol. Biol. Cell.* 29:2303–2316. https://doi.org/10.1091/mbc.E18-05-0274

Schindelin, J., I. Arganda-Carreras, E. Frise, V. Kaynig, M. Longair, T. Pietzsch, S. Preibisch, C. Rueden, S. Saalfeld, B. Schmid, et al. 2012. Fiji: An open-source platform for biological-image analysis. *Nat. Methods.* 9:676–682. https://doi.org/10.1038/nmeth.2019

Schmitt, D.L., Y.-J. Cheng, J. Park, and S. An. 2016. Sequestration-mediated downregulation of de Novo purine biosynthesis by AMPK. *ACS Chem. Biol.* 11:1917–1924. https://doi.org/10.1021/acschembio.6b00039

Schmitt, D.L., A. Sundaram, M. Jeon, B.T. Luu, and S. An. 2018. Spatial alterations of de novo purine biosynthetic enzymes by Akt-independent PDK1 signaling pathways. *PLoS One.* 13:e0195989. https://doi.org/10.1371/journal.pone.0195989

Senda, M., and Y. Natsumeda. 1994. Tissue-differential expression of two distinct genes for human IMP dehydrogenase (E.C.1.1.1.205). *Life Sci.* 54:1917–1926. https://doi.org/10.1016/0024-3205(94)90150-3

Shen, Q.-J., H. Kassim, Y. Huang, H. Li, J. Zhang, G. Li, P.-Y. Wang, J. Yan, F. Ye, and J.-L. Liu. 2016. Filamentation of metabolic enzymes in *Saccharomyces cerevisiae*. *J. Genet. Genomics.* 43:393–404. https://doi.org/10.1016/j.jgg.2016.03.008

Simonet, J.C., A.L. Burrell, J.M. Kollman, and J.R. Peterson. 2020. Freedom of assembly: Metabolic enzymes come together. *Mol. Biol. Cell.* 31:1201–1205. https://doi.org/10.1091/mbc.E18-10-0675

Spellicy, C.J., S.P. Daiger, L.S. Sullivan, J. Zhu, Q. Liu, E.A. Pierce, and S.J. Bowne. 2007. Characterization of retinal inosine monophosphate dehydrogenase 1 in several mammalian species. *Mol. Vis.* 13:1866–1872.

Stoddard, P.R., E.M. Lynch, D.P. Farrell, A.M. Dosey, F. DiMaio, T.A. Williams, J.M. Kollman, A.W. Murray, and E.C. Garner. 2020. Polymerization in the actin ATPase clan regulates hexokinase activity in yeast. *Science.* 367:1039–1042. https://doi.org/10.1126/science.aay5359

Suloway, C., J. Shi, A. Cheng, J. Pulokas, B. Carragher, C.S. Potter, S.Q. Zheng, D.A. Agard, and G.J. Jensen. 2009. Fully automated, sequential tilt-series acquisition with Leginon. *J. Struct. Biol.* 167:11–18. https://doi.org/10.1016/j.jsb.2009.03.019

Tan, Y.Z., P.R. Baldwin, J.H. Davis, J.R. Williamson, C.S. Potter, B. Carragher, and D. Lyumkis. 2017. Addressing preferred specimen orientation in single-particle cryo-EM through tilting. *Nat. Methods.* 14:793–796. https://doi.org/10.1038/nmeth.4347

Thomas, E.C., J.H. Gunter, J.A. Webster, N.L. Schieber, V. Oorschot, R.G. Parton, and J.P. Whitehead. 2012. Different characteristics and nucleotide binding properties of inosine monophosphate dehydrogenase (IMPDH) isoforms. *PLoS One.* 7:e51096. https://doi.org/10.1371/journal.pone.0051096

Wada, Y., A. Tada, T. Itabashi, M. Kawamura, H. Sato, and M. Tamai. 2005. Screening for mutations in the IMPDH1 gene in Japanese patients with autosomal dominant retinitis pigmentosa. *Am. J. Ophthalmol.* 140:163–165. https://doi.org/10.1016/j.ajo.2005.01.017

Wang, P.-Y., W.-C. Lin, Y.-C. Tsai, M.-L. Cheng, Y.-H. Lin, S.-H. Tseng, A. Chakraborty, and L.-M. Pai. 2015. Regulation of CTP synthase Filament Formation during DNA endoreplication in *Drosophila*. *Genetics*. 201:1511–1523. https://doi.org/10.1534/genetics.115.180737

Xu, D., G. Cobb, C.J. Spellicy, S.J. Bowne, S.P. Daiger, and L. Hedstrom. 2008. Retinal isoforms of inosine 5′-monophosphate dehydrogenase type 1 are poor nucleic acid binding proteins. *Arch. Biochem. Biophys.* 472:100–104. https://doi.org/10.1016/j.abb.2008.02.012

Zhao, H., C.R. Chiaro, L. Zhang, P.B. Smith, C.Y. Chan, A.M. Pedley, R.J. Pugh, J.B. French, A.D. Patterson, and S.J. Benkovic. 2015. Quantitative analysis of purine nucleotides indicates that purinosomes increase de novo purine biosynthesis. *J. Biol. Chem.* 290:6705–6713. https://doi.org/10.1074/jbc.M114.628701

Zhong, J., C.-J. Guo, X. Zhou, C.-C. Chang, B. Yin, T. Zhang, H.-H. Hu, G.-M. Lu, and J.-L. Liu. 2022. Structural basis of dynamic P5CS filaments. *Elife*. 11:e76107. https://doi.org/10.7554/eLife.76107
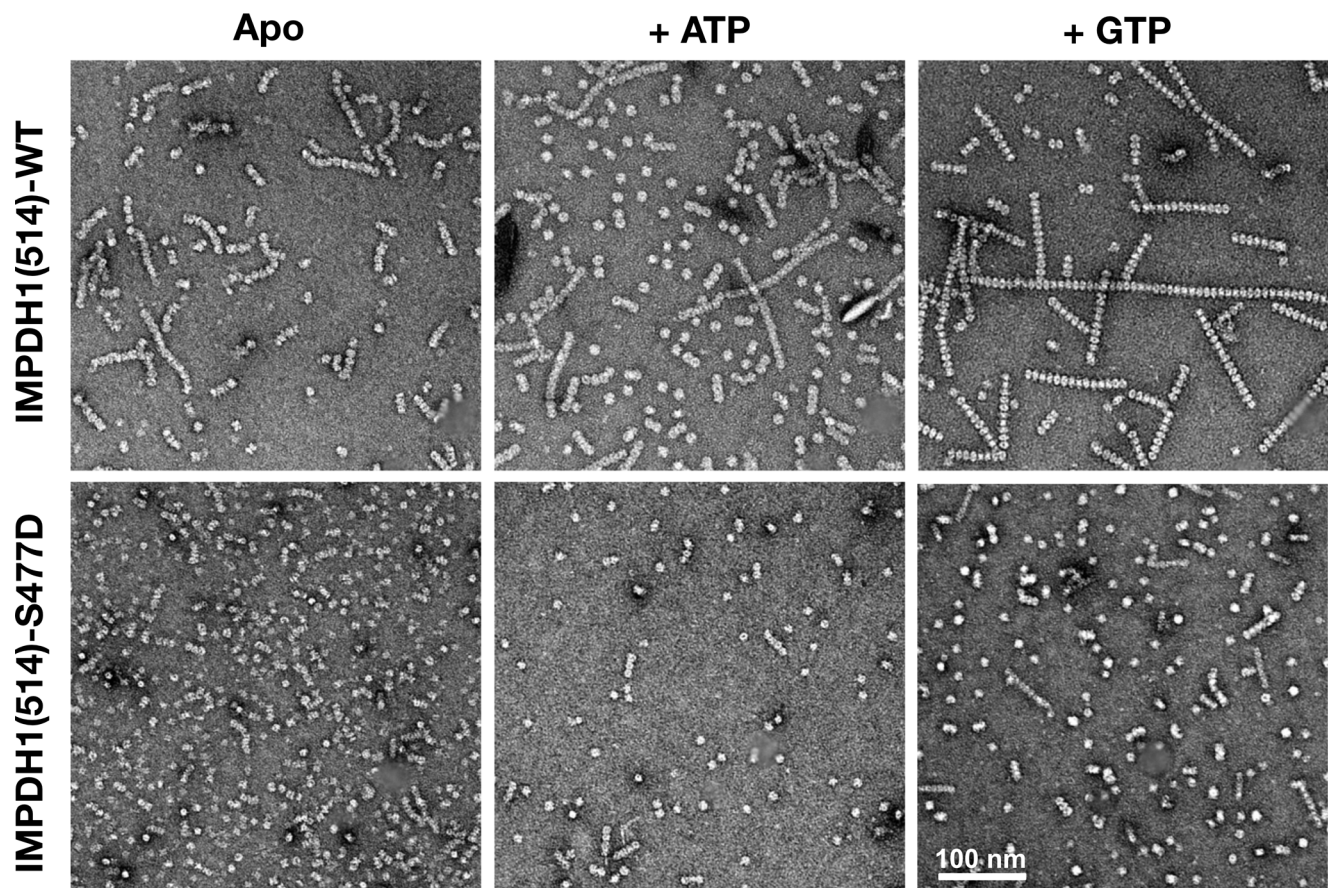
Figure S1. **S477D partially disrupts IMPDH1(514) filament assembly.** Negative stain EM of IMPDH1(514)-WT and IMPDH1(514)-S477D under Apo, +1 mM ATP, or +1 mM GTP conditions at 1 µM enzyme concentration.
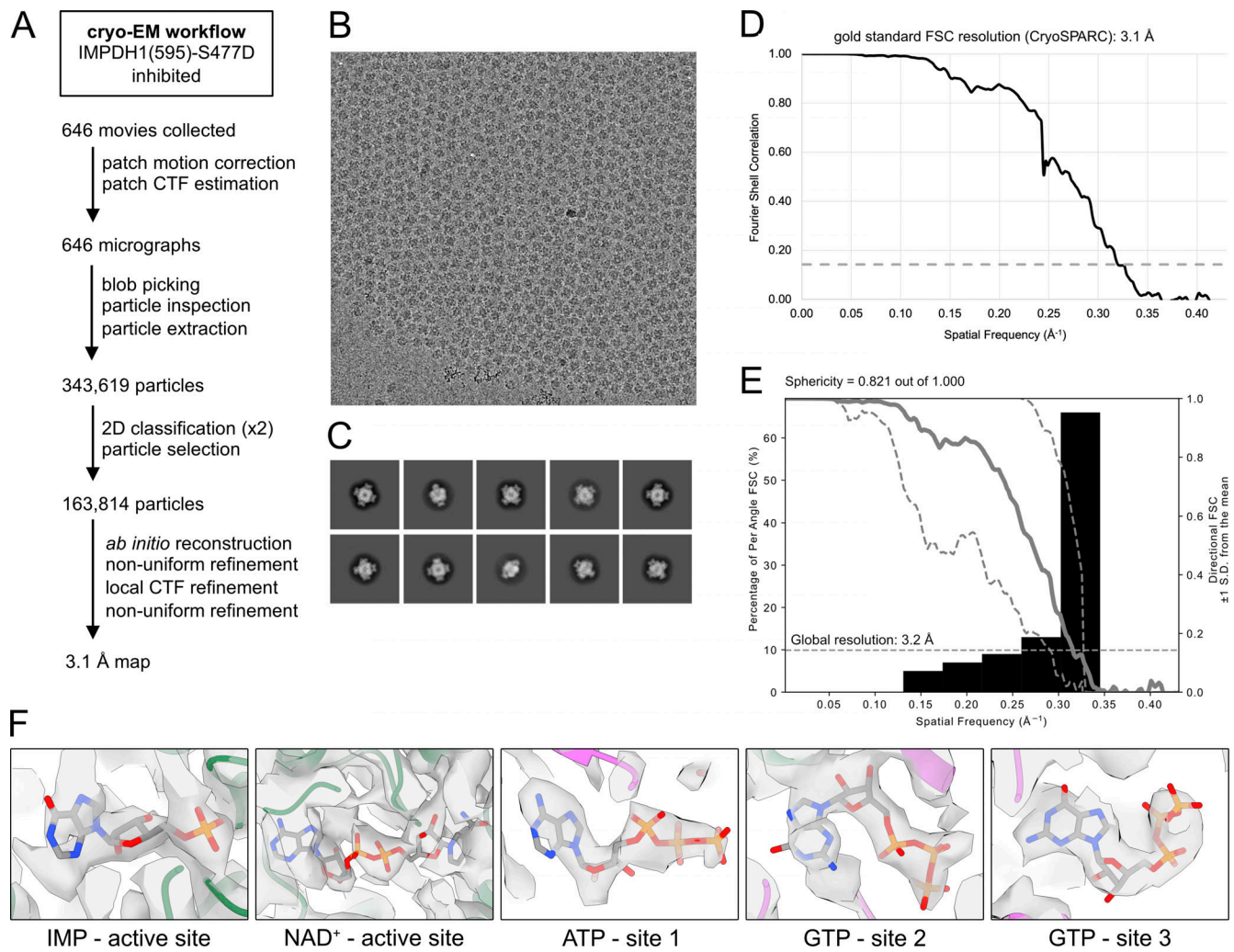
Figure S2. **Cryo-EM workflow for the inhibited IMPDH1(595)-S477D structure. (A)** Summarized data processing workflow. **(B)** Example micrograph. **(C)** Example 2D classes. **(D)** FSC curve from CryoSPARC. **(E)** Directional FSC plot depicting significant preferred orientation of the free octamer in ice. **(F)** Densities (gray) for bound ligands. Green: catalytic domain, pink: Bateman domain, red: oxygen, blue: nitrogen, orange: phosphorus.
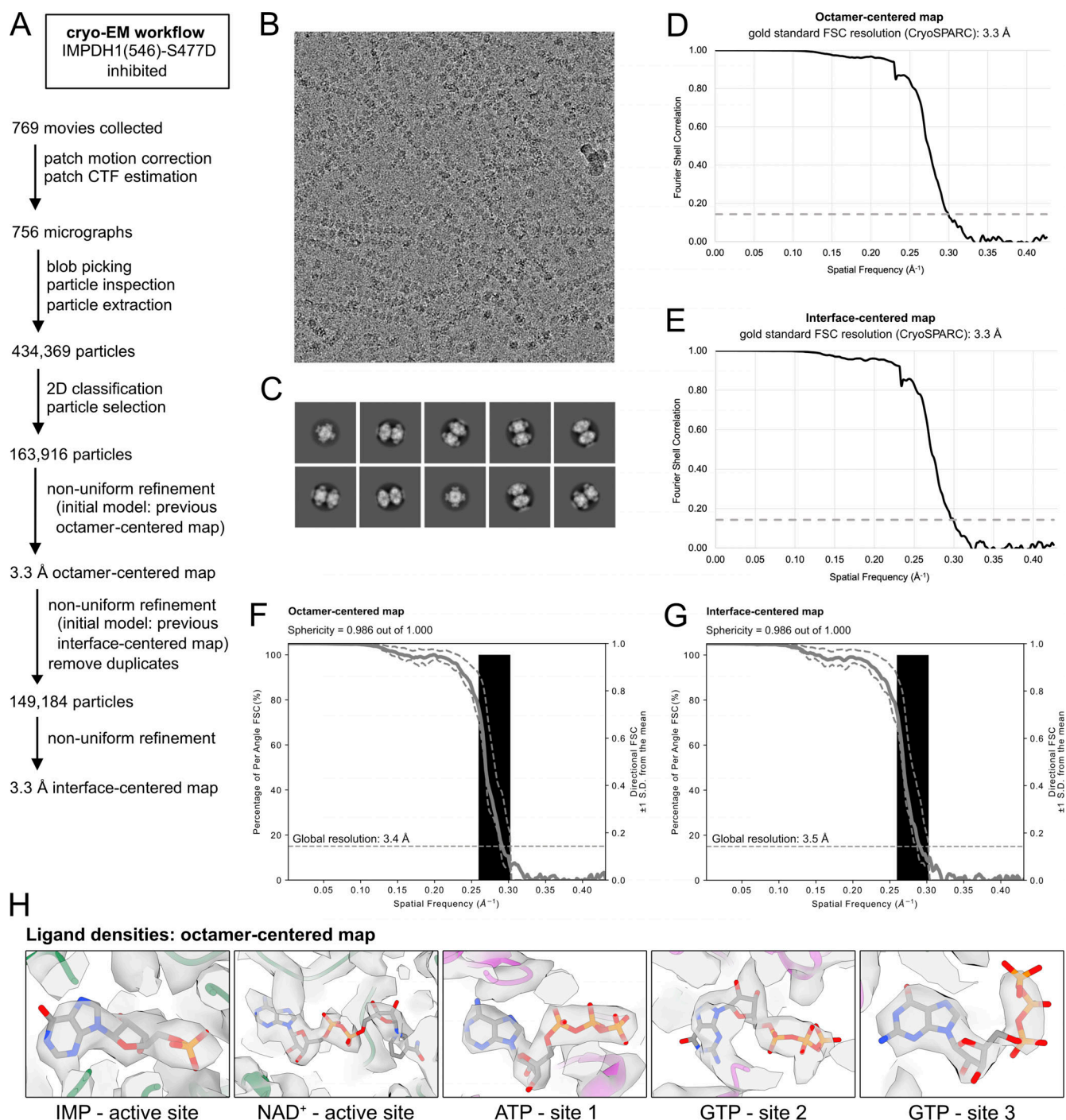
Figure S3. **Cryo-EM workflow for the inhibited IMPDH1(546)-S477D structures. (A)** Summarized data processing workflow. **(B)** Example micrograph. **(C)** Example 2D classes. **(D and E)** FSC curves from CryoSPARC for octamer-centered and interface-centered maps. **(F and G)** Directional FSC plots for octamer-centered and interface-centered maps. **(H)** Densities (gray) for bound ligands from the octamer-centered map. Green: catalytic domain, pink: Bateman domain, red: oxygen, blue: nitrogen, orange: phosphorus.
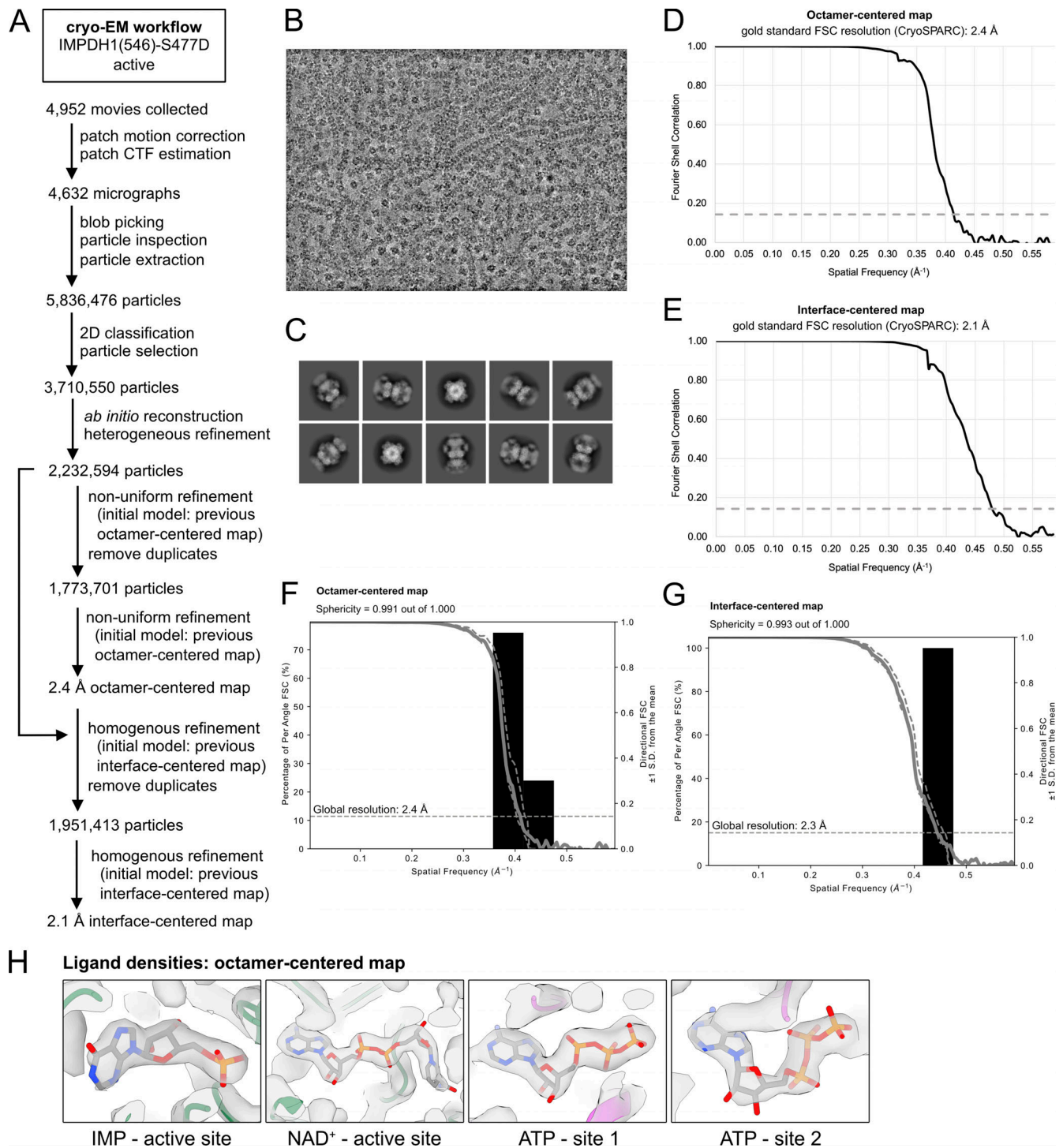
Figure S4. **Cryo-EM workflow for the active IMPDH1(546)-S477D structures. (A)** Summarized data processing workflow. **(B)** Example micrograph. **(C)** Example 2D classes. **(D and E)** FSC curves from CryoSPARC for octamer-centered and interface-centered maps. **(F and G)** Directional FSC plots for octamer-centered and interface-centered maps. **(H)** Densities (gray) for bound ligands from the octamer-centered map. Green: catalytic domain, pink: Bateman domain, red: oxygen, blue: nitrogen, orange: phosphorus.
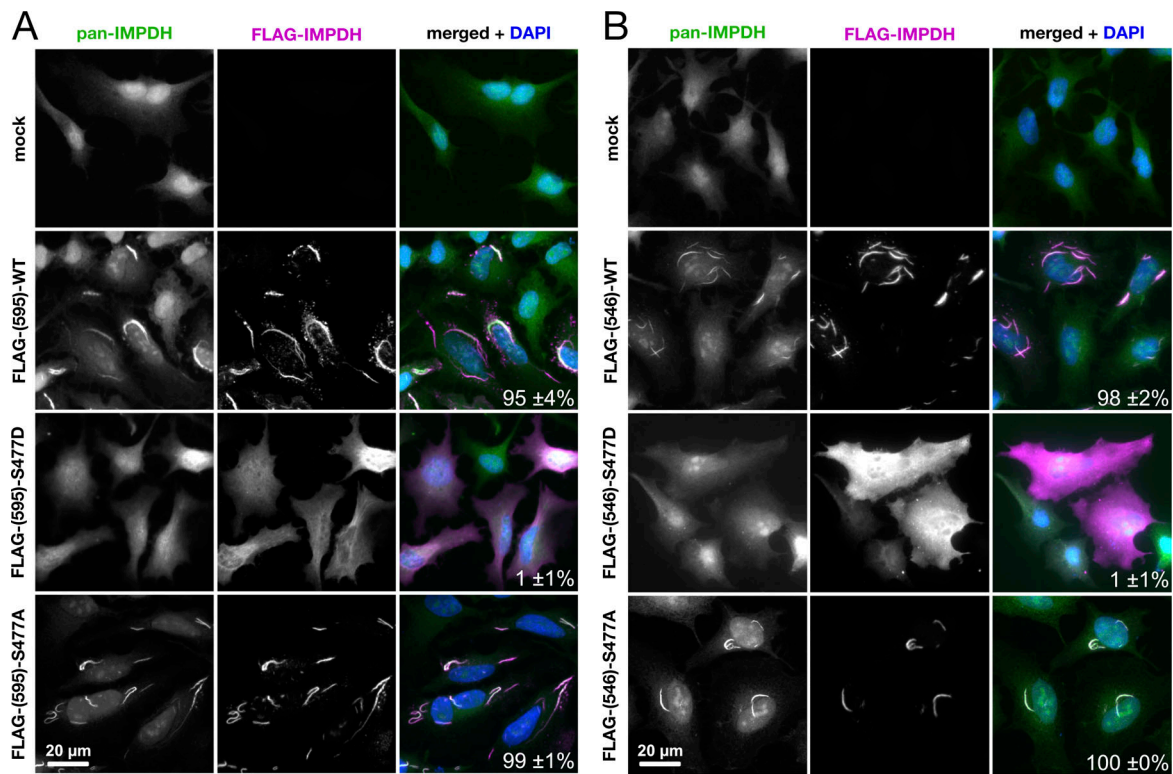
Figure S5. **S477D disrupts filament assembly in cells without ribavirin treatment. (A)** HeLa cells were transfected with FLAG-tagged IMPDH1(595)-WT, IMPDH1(595)-S477D, or IMPDH1(595)-S477A. Overexpression of the WT and S477A mutant induced filament assembly, but S477D did not. Mock transfection is shown as a control. Green: all IMPDH (endogenous + transfected). Magenta: FLAG-tagged fusion proteins. Blue: nuclei stained with DAPI. Percentage of transfected cells containing filaments is displayed in the bottom right corner of merged panels. **(B)** Same experiment as in panel A, but with FLAG-tagged IMPDH1(546)-WT, IMPDH1(546)-S477D, and IMPDH1(546)-S477A. Experiments were performed twice.